

Master's Thesis

Electromagnetic Analysis of Reflector Antenna Surfaces

Erik Sedhed



Electromagnetic Analysis of Reflector Antenna Surfaces

Department of Electrical and Information Technology Faculty of
Engineering, LTH, Lund University,
SE-221 00, Lund, Sweden



LUND
UNIVERSITY

Author:

ERIK SEDHED

Supervisors:

Andreas Ericsson
Niklas Wellander

Examiner:

Daniel Sjöberg

January 2015

Abstract

This master thesis investigates the electromagnetic reflection properties in the frequency range of 10-30 GHz of a tri-axial carbon fibre weave, with the strings rotated 60 degree to each other. The reflection performance is compared to a design requirement of having a reflection coefficient > -0.1 dB.

Some of the results in this report are calculated from the solution of the electromagnetic wave equation, which is solved numerically by the finite elements method in the frequency domain. To minimise the computational load modelling the weave, a thorough search for electromagnetically valid symmetries is done in order to find the smallest possible computational region to represent the entire weave.

The report includes a parametric sweep of the geometrical dimensions of the weave, the conductivity of the carbon fibre, the angle of incidence and the plane of incidence, in order to determine their influence on the reflection properties of the weave.

Two reflection enhancing improvements were considered; PEC coating and dual weave layers. As part of the dual weave work a method to describe the periodicity in the appearing moiré pattern was developed. It was found that the periodicity as function of rotation angle only exists when the cosine of rotational angles is a rational number. The work led to the discovery of quasi periodicity in moiré patterns. Furthermore, a method was developed to approximate the scattering matrix for a dual weave based on numerical simulations.

As final part of the report a comparison of a PEC parabolic reflector and a carbon fibre parabolic reflector is done based on physical optics and a modification of the physical optics approximation.

In this study, for given dimensions of the weave and with a carbon fibre conductance of 10^5 S/m, it could be concluded that a single weave did not meet the design requirement and that a suitable design, which does meet the design requirement, is the dual weave design. It could also be concluded that a parabolic reflector antenna with a surface reflection coefficient of -0.1 dB performs almost equally well as a PEC reflector.

Contents

Abstract	i
Contents	ii
1 Project description	1
1.1 The methodology of analysing the reflector surface	1
1.2 The weave	2
1.2.1 The weave strings	3
1.3 Full wave simulation and scattering matrix	3
1.4 Outline of the report	5
2 Satellites and the space antenna environment	6
2.1 Antenna environment	6
2.1.1 Radiation environment	6
2.1.2 Atomic oxygen	7
2.1.3 Contamination	7
2.1.4 Thermal environment	7
2.1.5 Launch environment	8
2.2 Orbits	8
2.3 Satellite types	9
2.3.1 Communications Satellites	9
2.3.2 Remote Sensing Satellites	9
2.3.3 Navigational Satellites	9
2.4 Satellite designing aspects	10
2.4.1 The spacecraft	10
2.4.2 Spacecraft budget	10
2.4.3 Satellite command and control link	10
2.4.4 Satellite positioning	10
2.4.5 Passive intermodulation, PIM	11
2.5 Satellite communication bands	11
2.5.1 UHF satellite communications antennas	11
2.5.2 L and S band communication satellite antennas	11
2.5.3 C-, Ku- and Ka-band FSS/BSS Antennas	12
2.6 Additionally	12
2.6.1 Faraday's effect in the ionosphere	12
3 Light weight antennas, mesh antennas and carbon fibre	13
3.1 Reflector antenna constructions	13
3.2 Previous work	14
3.3 Known material parameters	14

4	Weave geometry and electromagnetic symmetries	15
4.1	Introduction	15
4.2	Geometrical symmetries	15
4.2.1	Rotational symmetries	15
4.2.2	Mirroring symmetries	16
4.3	Requirements of electromagnetic symmetries in context of geometrical symmetries	17
4.3.1	Observation of periodicity	17
4.3.2	Electromagnetic mirror symmetries	18
4.4	Requirements for modelling an anisotropic material as isotropic in 2D	19
4.5	Numerical investigation of symmetries	20
4.5.1	Outcomes, numerical computations	21
4.6	Theoretical discussion	24
4.7	Summary	24
5	Parameter sweeps of the slab model	25
5.1	Introduction	25
5.2	Simulation model	25
5.3	Results	26
5.3.1	Validation of symmetries	26
5.3.2	Parametric sweep	27
5.3.3	Incidence angle sweep	28
5.3.4	Further observations	31
5.3.5	Power losses	32
5.4	Summary	33
6	Coating	35
6.1	Introduction	35
6.2	Method and results	35
6.3	Summary	37
7	Dual weave arrangements	38
7.1	Introduction	38
7.2	An analytical and numerical approach to understanding the moiré pattern	39
7.2.1	Derivation of a method	40
7.2.2	Periodicity	41
7.2.3	Relative hole area	43
7.3	Approximation at a macroscopic scale	45
7.3.1	Relative translation	46
7.3.2	Relative rotation	49
7.3.3	Both relative translation and rotation	54
7.4	Parametric sweep of the hole size in the dual weave case	54
7.5	Further observations	55
7.6	Summary	57

8	Parabolic reflector	58
8.1	Physical optics and parabolic antenna	58
8.2	Extension of the PO method	60
8.2.1	A useful expression	60
8.2.2	Derivation of method	60
8.3	Results	63
8.4	Summary	65
9	Conclusions	66
9.1	Conclusions relevant for the co-optimisation project	67
	Bibliography	68
	Appendices	70
A	Geometry appendix	71
B	Curls in the electric field in the slab model	73

1

Project description

This master thesis is a part of a major project within NRFP2, which stands for Nationellt rymdtekniskt forskningsprogram (National space technology research program). The project is a co-operation of Lunds Tekniska Högskola, KTH Royal Institute of Technology, and RUAG Space AB.

Background to the project

During the launch of satellites into space the satellite experiences a very high acoustical load with intensities of up to 148 dB. Throughout the lifetime of the satellite the launch and its acoustical loads is one of the major impacts of the antenna structure.

Another important issue with satellites is the cost of getting mass into orbit. It is very expensive and for this reason the total mass of the spacecraft is always a desirable parameter to minimise.

To reduce the possible damage during the launch and to minimise the total mass of the antenna a triaxial carbon-fibre weave design was suggested. The project as such is then a co-optimisation of the acoustic and electromagnetic properties of the triaxial carbon-fibre weave surface in the context of a reflector antenna in the frequency range of 10-30 GHz.

1.1 The methodology of analysing the reflector surface

To fully understand and evaluate the properties of this antenna design there are several levels that need to be thoroughly investigated. In Figure 1.1 these levels are presented in a schematic manner. Since the behaviour of the antenna will be very complicated to analyse taking all details down to a microscopic level in account, some valid approximations and simplifications must be done.

One simplification is to homogenise the conductivity of the strings in the weave. A further simplification is consider the weave to be a conducting slab by neglecting the insulation layer in-between the strings and its 3D structure.

Another coarser simplification is to homogenise the conductance of the entire unit cell and then calculate the reflection coefficient based on transmission line theory. This is done in [6]. This approximation is only valid at lower frequencies.

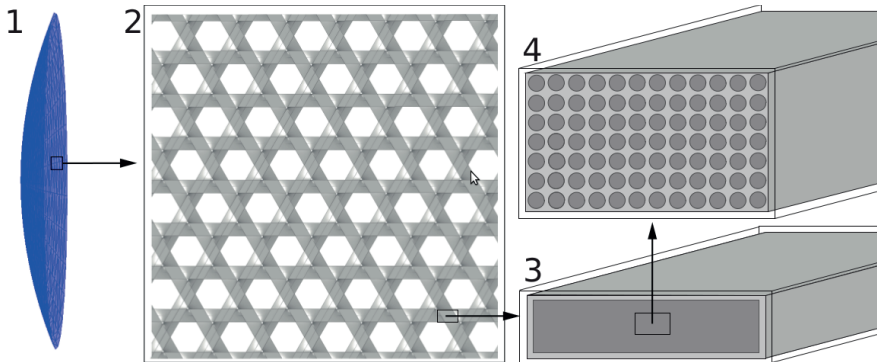


Figure 1.1: Schematic picture of different levels needed to be analysed in order to completely understand the carbon fibre antenna. 1. An example of an antenna shape [\sim m]. 2. The surface appearance of the carbon fibre weave [\sim mm]. 3. A string of the weave [$\sim 100 \mu\text{m}$]. 4. The conducting core of a carbon fibre and surrounding insulating glue [$\sim \mu\text{m}$].

1.2 The weave

For the reason mentioned in the background above, a certain carbon fibre weave was provided to be analysed. Its dimensions were not entirely set, but limited to be triaxial with a $\pi/3$ relative rotation. The reason for this choice is that the triaxial construction is mechanically strong, behaves rather isotropically and this type of weave is already being mass produced.

Let us define some parameters of the weave in context of a unit cell from which the entire weave can be constructed. Let $2a$ be the length of a side in the rhomboid shaped unit cell, b the length of one side in the hexagon shaped hole, w be the width of the strings and t is the thickness of the strings, see Figure 1.2.

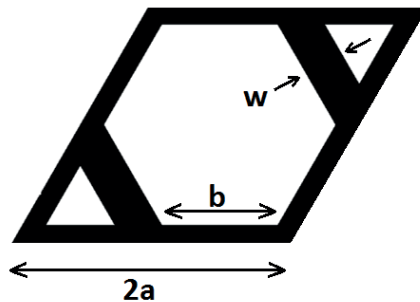


Figure 1.2: The unit cell of the slab model with chosen parameter names.

It can also be shown geometrically that a, b and w are related as (1.1) and that there is a constraint of the dimension of b (1.2).

$$w = (a - b)\sqrt{3} \quad (1.1)$$

$$\frac{2a}{3} \leq b < a \quad (1.2)$$

Based on the provided weave, found data [6], and Chapter 3, the parameters are likely to be around $a = 1$ mm, $\sigma = 10^4$ to 10^5 S/m and $t \approx 80$ μm . In appendix A some points in this unit cell are calculated and tabulated.

From previous work [6] it is shown that the weave can be represented by parallelogram shaped unit cells with periodic boundary conditions. Two cases are considered; the more accurate "fine structure" representation and the "slab" representation, see Figure 1.3.

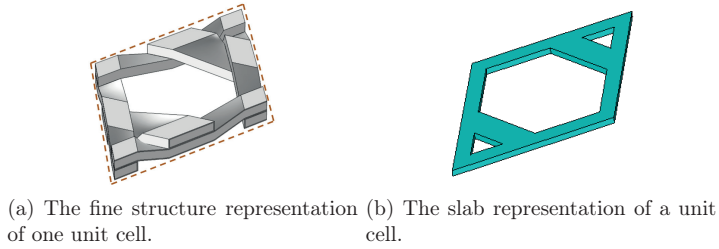


Figure 1.3: Weave models implemented in [6]

1.2.1 The weave strings

The weave is woven of strings. These strings consist of many thin carbon fibres that are glued together with an insulating glue. The strings are coated with an insulating layer, which prevents any currents from flowing from one string to another. See Figure 1.1.3-1.1.4.

In [6, Ch.2.4] is a thorough description of a homogenisation method of the string. The result of the homogenisation is that there is only conductivity along the fibre direction and that the conductivity is proportional to the fibre conductivity and its cross-sectional area, see (1.3).

$$\sigma_{\text{eff}} = \begin{pmatrix} 0 & 0 & 0 \\ 0 & 0 & 0 \\ 0 & 0 & \sigma_c A_c \end{pmatrix} \quad (1.3)$$

where σ_c is the conductivity of the fibre bundle per unit cell area in the string, A_c is the surface fraction of the conducting part of the unit cell.

1.3 Full wave simulation and scattering matrix

A main tool used to compute some of the results in this report are the electromagnetic computation programs Comsol and CST STUDIO SUITE. To future reference by

solving the "full wave" problem, it is referred to as numerically by the finite elements method computing the wave equation derived from Maxwell's equation.

$$\nabla \times (\nabla \times \mathbf{E}) - k_0^2 \mu_r \left(\epsilon_r - \frac{j\sigma}{\omega \epsilon_0} \right) \mathbf{E} = \mathbf{0} \quad (1.4)$$

The scattering matrix, reflection coefficient and phase change are often referred to in this project. The scattering matrix contains the information of how the incident electric field is reflected or transmitted. This is numerically computed in the programs by defined ports with different, orthogonal polarisations in the x- and y-direction, see Figure 1.4.

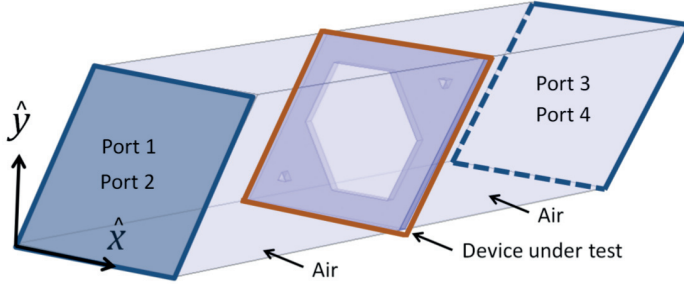


Figure 1.4: Explanation of the port arrangement used to compute the scattering matrix for a given problem. The figure is taken from [6].

The scattering matrix maps the incident electric field in each port with the scattered electric field by (1.5).

$$\mathbf{E}^{\text{out}} = \mathbf{S} \mathbf{E}^{\text{in}} \quad (1.5)$$

where the scattering matrix, \mathbf{S} , is given by (1.6). With 4 ports the \mathbf{E}^{out} in (1.5) consist of 4 components, describing the tangential electric field at each port.

$$\mathbf{S} = \begin{pmatrix} S_{11} & S_{12} & S_{13} & S_{14} \\ S_{21} & S_{22} & S_{23} & S_{24} \\ S_{31} & S_{32} & S_{33} & S_{34} \\ S_{41} & S_{42} & S_{43} & S_{44} \end{pmatrix} \quad (1.6)$$

where S_{12} means the complex scattering value mapping the incident E-field entering from port 2 with associated polarisation to the reflected E-field leaving through port 1 with associated polarisation. This follows the general convention of the scattering matrix and is also explained in [6]. Each element of the matrix consists of a complex number. The reflection coefficient of a certain polarisation is then the value of the associated scattering matrix element, and the phase shift due to the interaction with a media is the argument of the same complex number. The phase shift also depends on the relative position of the exciting port in the numerical programs, which must be taken into account computing the phase shift. The S-parameter in dB is calculated by the convention in (1.7).

$$S_{ij}^{\text{dB}} = 20 \log_{10}(|S_{ij}|) \quad (1.7)$$

1.4 Outline of the report

This master thesis report starts with a brief summary of the space environment in Chapter 2, how this impacts the satellite antenna design and general satellite and space antenna concepts. Chapter 4 aims to find the smallest possible computational region that can model the entire weave. The reason for this is to minimise the computational load and time, but still get the highest possible accuracy out of the numerical computations. In Chapter 5 parametric sweeps are conducted of the dimensions of the single layer weave, the conductivity of the weave fibers and different oblique angles of incidence. Chapters 6 and 7 investigate how much the performance of the weave improves by adding a PEC coating layer to the weave or by having two weaves placed on top of each other. Chapter 8 is a visualisation of how the obtained results in Chapter 5 impact the performance of a reflector antenna compared to a corresponding PEC reflector.

2

Satellites and the space antenna environment

2.1 Antenna environment

The near earth space environment differs significantly from the one at the surface of the earth and is in this context rather extreme. Examples of this are that the radiation is much higher, presence of vacuum, zero gravity due to orbiting and large and fast temperature changes.

The protective mechanisms of the earth's magnetic field and dense atmosphere that gives a stable temperature and lower radiation are not as present in the satellite environment and these mechanism can even counteract the protection. Due to these mechanisms the radiation can even be higher compared to deep space and the environment even more corrosive than on earth.

2.1.1 Radiation environment

Radiation belts

The radiation belts are regions relatively close to the earth that contain charged particles such as protons and electrons, which are trapped in the earth's magnetic field. The electrons move with an energy of a few MeV and the protons with an energy of several hundred MeV. The radiation belt has higher radiation flux at some spots closer to the earth, located at the poles and in the South Atlantic. The existence of the polar cones are due to the magnetic poles of the earth. The South Atlantic Anomaly (SAA) is due to the fact that the magnetic poles are not coincident with the rotational axis of the earth [9, p. 107].

Cosmic Rays

A summary of cosmic rays is that they originate outside the solar system and contain a low flux of particles, but include heavy, energetic (HZE) ions [9, p. 108]. The main sources of cosmic rays are stars and supernovas [14, chp. 3]. From the energy spectrum of the cosmic rays, it can be concluded that the energy per nucleon spans an interval from 100 MeV up to energies as high as 10^4 GeV. The differential flux is however more than 10^9 times higher for the lower energies, than for the higher ones [14, p. 112].

The plasma environment

The ionosphere consists, due to the high exposure of ultra violet (UV) light, of a plasma. An object located in a plasma is subject to a flux of charges. Since a plasma contains equally electric charge of electrons and ions and electrons are more mobile than the ions, a net flux of negative (with respect to the surrounding plasma) surface charge is often observed at objects located in a plasma. This flux is enhanced due to the effect of ionising radiation such as solar UV light or other previously mentioned radiation. The electrostatic charge can thereby often be modelled as a function of the plasma energy distribution, sunlit area and spacecraft surface materials. In order to minimise the electrostatic charge, one selects a surface material with high dielectric thickness and resistivity [9, p. 109].

The consequences of this phenomenon are that at high altitude the effect of the electrostatic charging is more noticeable, whilst at low altitude the plasma normally is cold and dense, causing the plasma to effectively conduct away any electric field from the spacecraft [9, p. 109].

2.1.2 Atomic oxygen

Due to the intense solar UV radiation of the ionosphere, atomic oxygen is present. This is especially problematic at lower altitudes since the atmosphere is more dense at lower altitudes. The presence of atomic oxygen varies throughout the day, because of its dependence on UV light.

The issue with atomic oxygen is that it is very reactive and corrosive. There are methods to reduce the impact of atomic oxygen, in order to increase the material durability of a spacecraft. One of them is to coat the material with SiO_2 , Al_2O_3 , indium tin oxide, Ge, Si, Al and Au [9, p. 110].

2.1.3 Contamination

Another issue is the problem of contamination. Studies have shown that the main source of contamination is the satellite itself in the form of eg. propellant gas and out-gassing of spacecraft materials. Other sources of contamination are micrometeoroids, orbital debris and space environment interactions with materials such as atomic oxygen [9, p. 110-111].

2.1.4 Thermal environment

The thermal conditions on a spacecraft orbiting earth can variate extremely, which can expose the space craft to corollary extreme strains and stresses if it is not properly constructed. The spacecraft temperature typically varies between -190 and 160 °C. The temperature variation is due to difference in energy of the sun exposure and the low temperature in space. Thus, it is possible that a slab that is exposed to the sun at one side has a very high temperature $\sim 160^\circ\text{C}$ and the backside has a very low temperature of $\sim -190^\circ\text{C}$, given that the slab conducts heat poorly. Another source of thermal variations is that most space-crafts orbit earth, leading to an oscillation back and forth from earth's shadow.

In [9, p. 112], it is stated that "Antennas must be protected by thermal hardware to limit the temperature range and gradients, and to control the heat exchange with the platform as well as the thermoelastic distortions". The methods used to protect the antenna are generally based on various methods of shielding, by e.g. coating and paint.

2.1.5 Launch environment

The most critical part of the spacecraft's lifetime is the launch phase. During the launch the spacecraft is exposed to different loads that originate from the propulsion system.

For larger exterior apertures of light weight and stiff architecture, such as an antenna, the acoustic load is one of the major loads at take off. The acoustic field can reach intensities as high as 148 dB and spans frequencies from 31.5 Hz to 2000 Hz [9, p. 113].

2.2 Orbits

There are essentially four different kinds of satellites orbiting the earth [9, p. 98-99];

- Low Earth Orbits (LEO) are located at an altitude of approximately 400 km and are often used for remote sensing satellites. The set back with LEO is that the very thin ionosphere causes a small draft and more presence of atomic oxygen. Similarly, there are also Medium Earth Orbits.
- Polar orbits are orbits that are orbiting the earth and always pass over the poles. This gives the advantage that the satellite eventually passes by the entire area of the earth, due to the rotation of the earth.
- Geostationary orbits are orbits where the satellite rotates with the same rotational speed in a circular orbit around earth, which results in that the satellite always dwells over the same spot on earth. They must be located above the equator at an altitude of approximately 36000 km (see Figure 2.1). There are currently more than 400 satellites orbiting earth in a geostationary orbit, giving a very limited angular separation of the satellites [9, p. 469].
- Highly elliptical orbits are described by Kepler's laws. The second law states that the area covered by line segment originating from the orbiting point will be constant per time unit for an object moving in a plane, orbiting a point. This implies that for very elliptical orbits, the object orbiting will spend more time furthest away from the earth. This fact is used to keep satellites for longer time over the northern respectively southern hemisphere.

A consequence of the satellite orbiting is the constant fall of the satellite, resulting in a zero gravity environment. This is important to be aware of when designing e.g. fuel systems, which can be solved by using a bladder tank [9, p. 102].

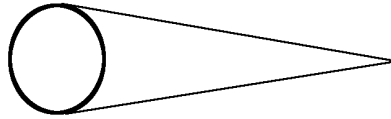


Figure 2.1: This figure illustrates the distance earth-geostationary satellite (~ 36000 km) in relation the size of earth. A satellite in LEO would in this picture appear to be located at the surface of earth.

2.3 Satellite types

2.3.1 Communications Satellites

There are various kinds of communications satellites [9, p. 77-79]. Below is a collection of some major groups of communication satellites;

- Fixed Satellite Service system (FSS) functions as a nodal point of a network, connecting places over a great distance with a radio link.
- Broadcast Satellite Services (BSS), also called Direct Broadcast Services (DBS) are used for e.g. television broadcasting. The system generally functions such that a broadcast centre transmits information to the satellite that then transmits the information over an area of the earth.
- Direct to Home Broadband Service (DTH) is very similar to BSS with the difference that it is a two-way connection.
- The last major group of communications satellites are the mobile communications Services. These systems are quite similar to the FSS systems with the difference that these satellites are shared by many more users.

2.3.2 Remote Sensing Satellites

Remote Sensing Satellites are used to analyse objects from far away. The main use of them is to detect and analyse things close to the surface of earth, but they can also be directed out to space as e.g. the Hubble space telescope.

An important subgroup of the remote sensing satellites are the radar satellites. The radar satellites are used for various tasks such as meteorology, earth science and aircraft tracking systems [9, p. 79].

2.3.3 Navigational Satellites

Navigational Satellites are very similar to communication satellites, such as the BSS, but requires additionally stable clocks. The global positioning system (GPS) is an example of a constellation of navigational satellites, which can be used to determine a ground position with very high precision [9, p. 79].

2.4 Satellite designing aspects

2.4.1 The spacecraft

A satellite is said to have two different groups of parts, the payload and the satellite bus. The payload is essentially all the active parts needed to perform the mission of the satellite and the satellite bus is all the other parts necessary to support the functionality of the payload. For e.g. a communication satellite, all the antennas and transponders would be part of the payload and the power supply system, attachment structure etc. would be part of the satellite bus [9, p. 100].

2.4.2 Spacecraft budget

Launching a satellite into space is a costly operation. Especially crucial for the total cost of the satellite is the total mass of the antenna, the power consumption and the thermal dissipation of the satellite [9, p. 101].

The mass aspect of the satellite is very much related to the cost of increasing the potential energy within the earth's gravitational field. The power consumption aspect is more of a factor related to the mission of the satellite. For e.g. a communication satellite a certain bandwidth require a certain power. To support this system one needs a power storage system and a power supply system (solar array). The capability of this combined system is very closely related to the total mass of the system and thus the cost to launch the satellite into orbit.

The third aspect of the satellite budget is the one of its thermal dissipation system. All the electronics in the satellite generate heat, which must be lead to the surface of the satellite to be radiated away. Thermal radiators require mass and are thereby directly related to the cost.

In the end all the costs are narrowed down to the total mass of the satellite. In order to optimise the cost of the satellite one should optimise the mass of the satellite and design related aspects to reach the required mission.

2.4.3 Satellite command and control link

Every satellite has a command and control system. The ground control must be able to communicate with the satellite in order to control and manoeuvre it, update software and for the satellite to respond with its current status and health [9, p. 80].

2.4.4 Satellite positioning

Since the gravitational field of earth is not uniform (the earth is slightly elliptic and its mass distribution is not homogeneous) and is disturbed mainly by the gravitational field of the moon and the sun, it is necessary to correct the orbit constantly. This correction is performed by pulse jets and requires brought fuel[9, p. 103].

Another aspect of the satellite that needs to be controlled is the orientation of the satellite. It is very important that the antennas are constantly directed in the proper direction, similarly important is it that the solar arrays and sensors are facing the proper direction. This is done by using various sensors keeping track of the earth's surface, stars, gravitational field and the sun [9, p. 104].

2.4.5 Passive intermodulation, PIM

In [5] the passive intermodulation is defined as:

"Passive Intermodulation is the unwanted generation of signals at several frequencies caused by the exposure of a passive component with non linear input/output characteristics to two or more RF signals. This phenomena can occur in contact junction, non similar metal contacts, corroded junctions, etc. It becomes a spacecraft problem primarily in common receive and transmit paths where the PIM frequency order falls within the receive band of the spacecraft."

In the context of high power equipment and satellites this phenomenon can cause major problems in the purity of the signal. The primary sources to PIM are formation of oxides, microcracks and contamination [15].

Since atomic oxygen is present in the satellite environment and it is very difficult to avoid impurity and microcracks in metals, coating and metal antenna structures are less desirable for satellite antenna constructions. This is also a reason to minimise any source of contamination of the antenna.

2.5 Satellite communication bands

2.5.1 UHF satellite communications antennas

Ultra high frequency is a frequency band covering between about 300 MHz to 1 GHz. To meet the typical designing requirement at these frequencies, an antenna with a rather high directivity is commonly realised as e.g. a helix antenna. If a higher gain is required, than the single element design can provide, one often put several single elements together to form an antenna array [9, p. 71-73].

2.5.2 L and S band communication satellite antennas

At higher frequencies (L- and S band spans from 1 GHz to 4 GHz) and for mobile satellite communication system (MSCS) purposes, a high-gain spot beam is wanted. In [9, p.468-469] the link budget of the satellite system is discussed in terms of the signal to noise ratio. It is concluded that for relatively low frequencies (as the L and S band represent in the satellite communication aspects) large apertures are needed to create good spot beams. Therefore most of these antennas are equipped with reflectors of the size of 6 m to more than 22 m [9, p. 474-476].

By feeding the reflector with antenna arrays, one can achieve a large number of beams covering half the surface of the earth facing the satellite. With modern digital signal processing, one can form a greater quantity of thinner beams. An important part of the beam cell separation is based on using different polarisations.

The enormous size of the reflector antennas (larger than 22 m in diameter) and the fact that they will be used in a "zero-gravity" environment make it really difficult to test their performance. Therefore mainly software implemented models are used to evaluate the satellite performance[9, p. 479].

2.5.3 C-, Ku- and Ka-band FSS/BSS Antennas

These bands span from 4 GHz to approximately 31.2 GHz.[9, p. 480] They also usually operate with reflector antennas in order to generate narrow beams, but due to the much higher frequency the size of these reflector antennas are smaller than for the L and S band communication satellites, up to 3 m [9, p. 482].

Gregorian Dual-Reflector geometry can be applied to reduce the losses due to cross polarisation [9, p. 486]. Current research is exploiting implementations of larger reflectors to be implemented in the Ka band, utilising massive active feed arrays.

2.6 Additionally

2.6.1 Faraday's effect in the ionosphere

It can be shown that an electromagnetic wave that propagates through plasma with a static magnetic field experiences the Faraday rotation effect. The effect causes a linearly polarised signal to rotate (appear to be circularly polarised) as it propagates through the plasma. When the signal exits the plasma it continues to be linearly polarised, but not necessarily in the same direction.

The effect in a plasma (angle of rotation) with an external static magnetic field for light propagating along the magnetic field lines can be summarised in the following equation;

$$\varphi = \frac{\omega_g \omega_p^2}{2c(\omega^2 - \omega_g^2)} z \quad (2.1)$$

where ω_g is the electron gyro-frequency, ω_p is the plasma frequency, c is the speed of light, ω is the frequency of the incident wave and z is the total distance travelled through the plasma [3, p. 401].

The ionosphere fulfils these required properties and exhibits the Faraday effect. It contains a plasma and is subject to earth's static magnetic field. An implication learned from (2.1) is that the angle of rotation depends very much on the frequency of the incident wave. Thus as the the frequency ω goes to infinity the angle of rotation goes to zero, which means that for higher frequencies, such as the C-, Ku- and Ka-band, this effect can be neglected [3, p. 399-401].

3

Light weight antennas, mesh antennas and carbon fibre

This chapter summarises a brief literature study done in order to get an overview of reflector antennas and what has been published on the topic light weight antennas and electromagnetic properties of carbon fibres.

3.1 Reflector antenna constructions

A recently popular reflector antenna construction is the sandwich construction. It is generally made by composite materials with an outer shell of e.g. carbon-fiber-reinforced polymer (CFRP) and in-between there is a supporting structure such as a honeycomb shaped material.

- **Thick shell reflector** is essentially only the sandwich antenna, without a supporting structure. This limits the maximum size of the reflector.
- **Thin shell reflector** is also a sandwich antenna, but with a supporting back structure. This allows the antenna to be thinner and yet larger than the thick shell reflector.
- **Ultra Light Reflector (ULR)** is very similar to the thin shell reflector, but with the modification that it has holes in the structure reducing the acoustical load and the total mass of the reflector.

There are also in contrast to the sandwich constructions other constructions:

- **Monolithic stiffened shells** which could be very similar to the thin shell reflector but without the in-between material. Thus it is only a shell with a supporting arch.
- **Dual-gridded reflectors (DGR)** are two reflectors in series with different inclination, where the outer one possesses a linear polarisation selectivity of the incident wave. The strength of this concept design is that the construction offers a method to reduce losses due to cross-polarisation and the possibility to separate vertically and horizontally polarised waves.

- **ULR** constructed by a pure mesh of e.g. a metal or a carbon fibre.

The information originates from [9, p. 136-142].

3.2 Previous work

The tri-axial carbon fibre weave was investigated in a study performed in 2003 by TICRA. It included development of a program, MESTIS, specifically developed for the purpose of evaluating the properties of up to three weaves. One approximation which is applied is that all the threads in the weave run in the same plane. The study was done for a weave with the string width and wavelength ratio was $1/200$. The study concluded that the reflection was almost independent on the azimuthal incident angle, but very much dependent on the polar incident angle [12].

A comparison of the performance of three different woven metallic meshes at the frequency of 20 GHz was done in 2004. A mesh called the single satin, had a transmission loss for normal incidence of -19 dB and it was pretty much independent of the direction of the wave polarisation [11].

The Northrop Grumman has published some measurements at the following webpage; [1, p. 7]. For frequencies spanning from 1.5-60 GHz, all the transmission losses were above -0.14 dB, partly depending on the knit density.

By using the given data in [9, p. 317-318], one can obtain an estimate of the density of a metal mesh reflector antenna. The first AstroMesh tension truss antenna from Northrop Grumman has a diameter of 12.25 m and a total mass of 55 kg, which gives an approximate density of $55/6.125^2\pi \approx 0,467$ kg/m².

3.3 Known material parameters

A measurement of the conductivity of carbon fibre in the frequency range of 0-12 GHz, resulted in values spanning from $5 \cdot 10^4$ S/m to about $9 \cdot 10^4$ S/m [8].

In a measurement of the reflection coefficient and conductivity of carbon fibre in 2010, it was shown that the reflection coefficient of the unidirectional CFRP laminate, in the frequency range of 8-12 GHz, is very high ($S_{11} \approx -1$) when the incident electric field is parallel to the fibre direction. It was also shown that the reflection coefficient is frequency dependent for the polarisation when the incident electric field is perpendicular to the fibre direction. For this case the reflection coefficient increases with frequency. Similarly, when the carbon fibre is quasi-isotropic, the reflection coefficient is very high, but slightly lower than when the incident E-field is parallel to unidirectional carbon fibre [7].

The conductivity of some commercially produced carbon fibre can be found on the companies' web-pages. The highest conductivity found was one produced by Toho Tenax. One of their carbon fibres has a conductivity of $1.03 \cdot 10^5$ S/m [2].

4

Weave geometry and electromagnetic symmetries

4.1 Introduction

To model a composite reflector antenna surface some approximations are utilised. One of these approximations is to model the structure as a 2D infinite structure. To numerically compute the reflection properties of this weave further approximations must be done. In order to get high accuracy in the numerical computations within a reasonable time, it is desirable to find the smallest possible computational region that represents the geometrical and electromagnetic properties of the weave correctly.

In this chapter the geometric symmetry properties of the weave are investigated, the electromagnetic requirements on found symmetries derived and finally the found results are confirmed by numerical computations. It is also shown that a weave made by three fibre directions of an anisotropic material with a $\pi/3$ offset can be approximated as an isotropic material.

4.2 Geometrical symmetries

By just considering the distribution of material in the weave (represented by the conductivity parameter $\sigma(\mathbf{x})$) one can identify some geometrical symmetries. These results are not just crucial for reducing the size of the computational region which represents the weave, but are also very useful to be aware of when drawing the object in a computer simulation program.

From previous work in [6] it is shown that the weave can be represented by parallelogram shaped unit cells with periodic boundary conditions. Two cases are considered; the more accurate "fine structure" representation and the "slab" representation, see Figure 1.3.

4.2.1 Rotational symmetries

Due to the fact that the tri-axial weave is made of fibres with a $\pi/3$ rotation with respect to each other, one would strongly suspect a rotational symmetry of $\pi/3$. Such a symmetry is found in the fine structure representation. It is also valid in the slab

representation, where it is even possible to reduce the unit cell size further by a factor 2. See Figure 4.1.

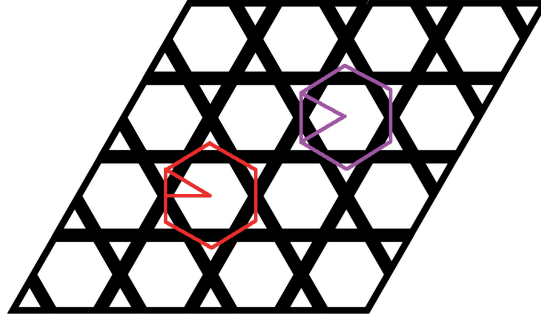


Figure 4.1: The purple symmetry is geometrically valid for both material representations. The red one is only valid in the slab model.

4.2.2 Mirroring symmetries

In the slab model, one can identify lines with respect to which the weave is symmetric. These symmetries can also be further reduced by identifying a π rotational symmetry, see Figure 4.2.

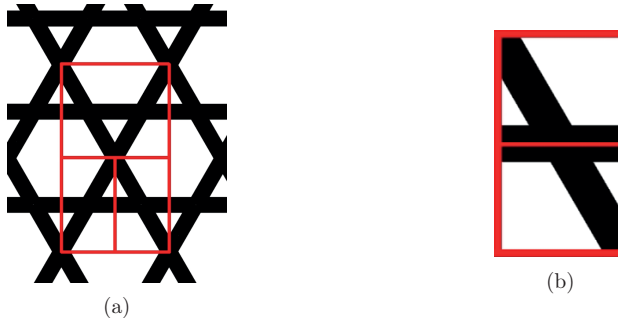


Figure 4.2: Lines of symmetry for the slab weave (a) and two rotational symmetries in the smallest mirroring symmetry (b).

By looking at the mathematical representation of the slab, it can easily be concluded that the symmetry lines in Figure 4.2(a) are fixed, given a certain unit cell size and are independent of the hexagon shaped hole size and weave string width. Similar mirroring symmetries could not be found in the fine structure weave due to the orientation of the strings.

4.3 Requirements of electromagnetic symmetries in context of geometrical symmetries

In order to mathematically prove the validity of the found symmetries the properties of some simple 2D models are investigated. The continuity equation (4.1) states that the flow of charges out of a volume must be equal to the change of charges within it.

$$\oint_S \mathbf{J} \cdot d\mathbf{A} = - \int_V \frac{\partial \rho}{\partial t} dV \iff \nabla \cdot \mathbf{J} = - \frac{\partial \rho}{\partial t} \quad (4.1)$$

Furthermore, Kirchhoff's expression of Ohm's law (4.2) is known as:

$$\mathbf{J} = \sigma \mathbf{E} \quad (4.2)$$

where σ is the conductivity of the material.

4.3.1 Observation of periodicity

To start with, there are some properties which can be observed in a periodic structure. Consider an infinite 2D region in the xy-plane, where the source distribution at a given point, \mathbf{x} , is given by the function $f(\mathbf{x}) = \frac{\partial \rho}{\partial t}$. Let \mathbf{p} be a vector describing a periodicity in the structure and assume that the source distribution holds this periodicity, that is (4.3):

$$f(\mathbf{x}) = f(\mathbf{x} + \mathbf{p}). \quad (4.3)$$

Similarly, due to the geometric symmetry with the same periodicity (4.4), describing the material distribution in the plane, must be true

$$\sigma(\mathbf{x}) = \sigma(\mathbf{x} + \mathbf{p}). \quad (4.4)$$

By inserting (4.2) in (4.1), one obtains:

$$-\nabla \cdot [\sigma(\mathbf{x})\mathbf{E}(\mathbf{x})] = f(\mathbf{x}) \quad (4.5)$$

Then by inserting (4.3) and (4.4) in (4.5) one can obtain the following observation:

$$-\nabla \cdot [\sigma(\mathbf{x} + \mathbf{p})\mathbf{E}(\mathbf{x})] = f(\mathbf{x} + \mathbf{p}) \quad (4.6)$$

the question to answer is what is the electric field in $\mathbf{E}(\mathbf{x} + \mathbf{p})$? Let $\mathbf{x} + \mathbf{p}$ in (4.5):

$$-\nabla \cdot [\sigma(\mathbf{x} + \mathbf{p})\mathbf{E}(\mathbf{x} + \mathbf{p})] = f(\mathbf{x} + \mathbf{p}) \quad (4.7)$$

Since the right hand side of (4.7) is equal to the right hand side of (4.6) one obtains:

$$-\nabla \cdot [\sigma(\mathbf{x} + \mathbf{p})\mathbf{E}(\mathbf{x})] = -\nabla \cdot [\sigma(\mathbf{x} + \mathbf{p})\mathbf{E}(\mathbf{x} + \mathbf{p})] \Leftrightarrow \mathbf{E}(\mathbf{x} + \mathbf{p}) = \mathbf{E}(\mathbf{x}) \quad (4.8)$$

Thus, if a structure consists of material that recurs with a given periodicity and has a source distribution with the same periodicity, the electric field is periodic.

4.3.2 Electromagnetic mirror symmetries

If one looks at a case of an incident wave of linear polarisation, one can represent the geometric mirroring symmetries in 2D by two parallel perfect electric conductors (PEC) which are orthogonal to two parallel perfect magnetic conductors (PMC). The PEC must also be orthogonal to the incident E-field. To show the electromagnetic requirements on the geometry of the material, the following reasoning can be done.

Consider the continuity equation (4.1). Let us define a connected set of points, which only contains points that are not periodic to each other within the set and that have a symmetry line cutting exactly the middle of the set. Let us load the cell with a potential difference between the boundaries that are orthogonal to the symmetry line. This is visualised in Figure 4.3. From Section 4.3.1 it is then shown that the boundaries of this set must be periodic to each other.

To use PMC at the boundaries parallel to the symmetry line the current flow through the boundaries must be zero. That is the homogeneous Neumann boundary condition: $\hat{\mathbf{n}} \cdot \sigma \mathbf{E} = 0$. This is fulfilled in the case of periodic boundaries in combination with introducing the constraint that the current density must be continuous, which mathematically avoids point current sources at the boundaries.

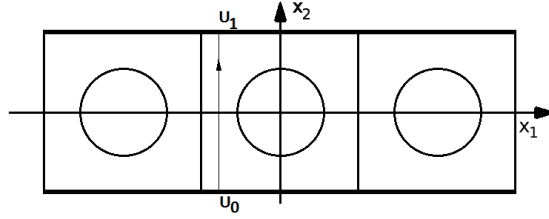


Figure 4.3: A row of unit cells loaded by a static electric field defined by the potentials U_0 and U_1 . In this example the x_2 -axis is the symmetry line.

Consider a symmetry line for which (4.9) and (4.10) are fulfilled for the x_1 -coordinate.

$$\sigma(-x_1, x_2) = \sigma(x_1, x_2) \quad (4.9)$$

$$f(-x_1, x_2) = f(x_1, x_2) \quad (4.10)$$

Then by using the continuity equation (4.1), (4.10), and assuming an isotropic material, one can argue:

$$\nabla \cdot [\sigma(x_1, x_2) \mathbf{E}(x_1, x_2)] = \nabla \cdot [\sigma(-x_1, x_2) \mathbf{E}(-x_1, x_2)] \quad (4.11)$$

That is:

$$\begin{aligned}
 -\nabla \cdot [\sigma(x_1, x_2)\mathbf{E}(x_1, x_2)] &= \\
 &= \frac{\partial}{\partial x_1}[\sigma E_1] + \frac{\partial}{\partial x_2}[\sigma E_2] = \\
 &= \sigma(x_1, x_2) \frac{\partial}{\partial x_1}[E_1(x_1, x_2)] + \frac{\partial}{\partial x_1}[\sigma(x_1, x_2)]E_1(x_1, x_2) + \\
 &+ \sigma(x_1, x_2) \frac{\partial}{\partial x_2}[E_2(x_1, x_2)] + \frac{\partial}{\partial x_2}[\sigma(x_1, x_2)]E_2(x_1, x_2) = f(x_1, x_2) \quad (4.12)
 \end{aligned}$$

Inserting $-x_1$ instead of x_1 gives:

$$\begin{aligned}
 -\nabla \cdot [\sigma(-x_1, x_2)\mathbf{E}(-x_1, x_2)] &= \\
 &= -\sigma(x_1, x_2) \frac{\partial}{\partial x_1}[E_1(-x_1, x_2)] - \frac{\partial}{\partial x_1}[\sigma(-x_1, x_2)]E_1(-x_1, x_2) + \\
 &+ \sigma(-x_1, x_2) \frac{\partial}{\partial x_2}[E_2(-x_1, x_2)] + \frac{\partial}{\partial x_2}[\sigma(-x_1, x_2)]E_2(-x_1, x_2) = f(-x_1, x_2) \quad (4.13)
 \end{aligned}$$

Due to (4.10), (4.12) must be equal to (4.13), one solution is:

$$\begin{cases} E_1(-x_1, x_2) = -E_1(x_1, x_2) \\ E_2(-x_1, x_2) = E_2(x_1, x_2) \end{cases} \quad (4.14)$$

We know from Section 4.3.1 that $-\nabla \cdot [\sigma\mathbf{E}] = f$ has a unique solution. Therefore the electric field is mirrored in the symmetry line, $x_1 = 0$, that is $E_1(-x_1, x_2) = -E_1(x_1, x_2)$. The right and left limit at the symmetry line must be consistent due to continuity:

$$\lim_{x_1 \rightarrow 0^-} -\nabla \cdot [\sigma(x_1, x_2)\mathbf{E}(x_1, x_2)] = \lim_{x_1 \rightarrow 0^+} -\nabla \cdot [\sigma(x_1, x_2)\mathbf{E}(x_1, x_2)] \Rightarrow E_1|_{x_1=0} = 0 \quad (4.15)$$

This means that the electric field must be parallel to the symmetry line along the symmetry line. Since the material is symmetric the whole reasoning can be shifted to the boundaries of the periodic element to show that the E-field must be parallel to these boundaries as well.

To summarise it: For a symmetric material that is delimited by a rectangle, where the symmetry line of the material is parallel to one of the sides of the rectangle, the material can correctly be modelled with two PEC and two PMC boundaries.

4.4 Requirements for modelling an anisotropic material as isotropic in 2D

This is a proof that a material can be approximated as a homogeneous isotropic material if it has three anisotropic directions with a $\pi/3$ rotation to each other within a plane.

Consider an arbitrary conductivity matrix for a 2D material (4.16)

$$\tilde{\sigma} = \begin{pmatrix} \sigma_{11} & \sigma_{12} \\ \sigma_{21} & \sigma_{22} \end{pmatrix}. \quad (4.16)$$

Also consider the electric field in the three directions (4.17).

$$\begin{cases} \mathbf{E}_1 = \begin{pmatrix} 1 \\ 0 \end{pmatrix} \\ \mathbf{E}_2 = \frac{1}{2} \begin{pmatrix} 1 \\ \sqrt{3} \end{pmatrix} \\ \mathbf{E}_3 = \frac{1}{2} \begin{pmatrix} -1 \\ \sqrt{3} \end{pmatrix} \end{cases} \quad (4.17)$$

The current density in each direction are defined by Ohm's law (4.2) and these electric fields (4.17), that is (4.18).

$$\begin{cases} \mathbf{J}_1 = \tilde{\sigma} \mathbf{E}_1 \\ \mathbf{J}_2 = \tilde{\sigma} \mathbf{E}_2 \\ \mathbf{J}_3 = \tilde{\sigma} \mathbf{E}_3 \end{cases} \quad (4.18)$$

Let us define the rotation matrix according to (4.19).

$$\mathbf{R}_{\pi/3} = \frac{1}{2} \begin{pmatrix} 1 & -\sqrt{3} \\ \sqrt{3} & 1 \end{pmatrix} \quad (4.19)$$

Due to the normalisation of the electric field, the $\pi/3$ rotation of a current density vector should result in one of the following.

$$\begin{cases} \mathbf{R}_{\pi/3} \mathbf{J}_1 = \mathbf{J}_2 \\ \mathbf{R}_{\pi/3} \mathbf{J}_2 = \mathbf{J}_3 \\ \mathbf{R}_{\pi/3} \mathbf{J}_3 = -\mathbf{J}_1 \end{cases} \quad (4.20)$$

The results of (4.20) are summarised in (4.21), as a system of equations.

$$\begin{cases} \sigma_{11} - \sqrt{3}\sigma_{21} = \sigma_{11} + \sqrt{3}\sigma_{12} \iff -\sigma_{21} = \sigma_{12} \\ \sqrt{3}\sigma_{11} + \sigma_{21} = \sigma_{21} + \sqrt{3}\sigma_{22} \iff \sigma_{11} = \sigma_{22} \\ 3\sigma_{12} - \sqrt{3}\sigma_{11} + \sqrt{3}\sigma_{22} - \sigma_{21} = 4\sigma_{21} \iff \sigma_{12} = \sigma_{21} \end{cases} \quad (4.21)$$

$$\begin{cases} \sigma_{12} = \sigma_{21} \\ -\sigma_{21} = \sigma_{12} \end{cases} \implies \sigma_{21} = \sigma_{12} = 0 \quad (4.22)$$

Thus the conductivity matrix, (4.16) must be:

$$\tilde{\sigma} = \sigma \begin{pmatrix} 1 & 0 \\ 0 & 1 \end{pmatrix} \quad (4.23)$$

Thereby an isotropic model is appropriate.

4.5 Numerical investigation of symmetries

In order to investigate the electromagnetic validity of the found geometrical symmetries, a numerical study was conducted. The boundaries of the symmetries should fulfil the known mirroring properties of PEC and/or PMC, that is at the boundaries the electric field is either parallel or orthogonal to the boundaries.

4.5.1 Outcomes, numerical computations

In Figure 4.5(b) one can see that the electric field lines that cross the boundaries of the $\pi/3$ rotational symmetry in most cases are not parallel or orthogonal to the boundaries. The settings of the boundary change for every section and it will therefore be very difficult to use this rotational symmetry to its full potential. An attempt to model this with PEC and PMC boundary conditions was done, but a method to describe the rotation correctly was not found.

In Figures 4.6 and 4.7 the electric field direction is plotted in the inner and outer tangential planes (orthogonal to the incident wave) of the fine structure weave. It is then shown that the electric field curl within the structure along geometrical symmetry lines. Thus it is not possible to represent the fine structure weave with a smaller element than the unit cell with periodic boundaries.

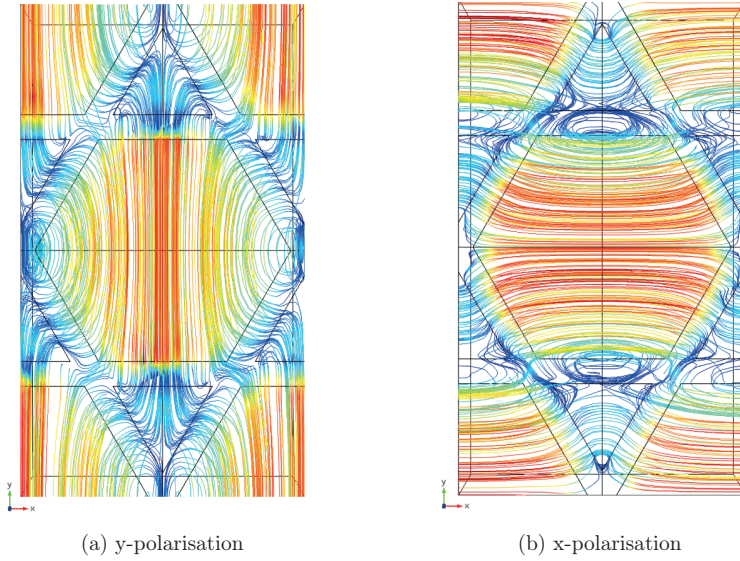


Figure 4.4: To numerically evaluate the found symmetries the computed electric field lines with the x and y polarised excitation were plotted respectively.

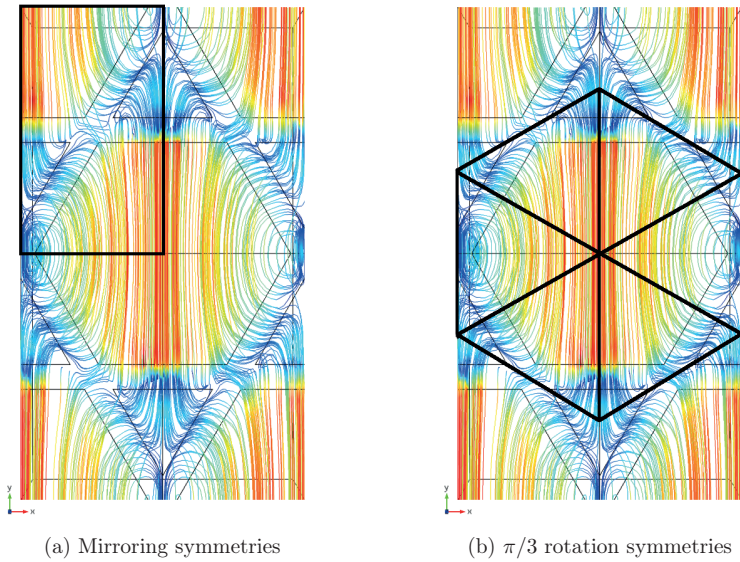


Figure 4.5: Same as Figure 4.4a, but with marked symmetry lines.

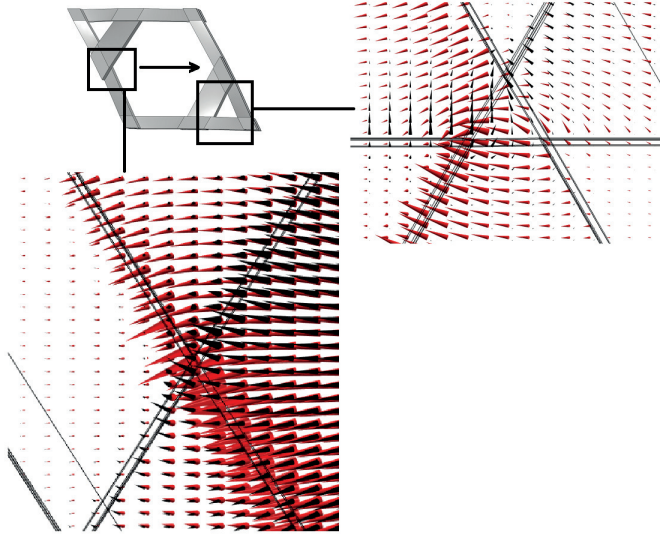


Figure 4.6: The red and black cones represent the direction of the electric field in the points located at the tangential plane closest to the source (red cones) and furthest away (black cones) in the fine structure weave. The arrow in the black unit cell displays the polarisation of the incident wave. Note that the field curls within the weave at a geometrical symmetry line.

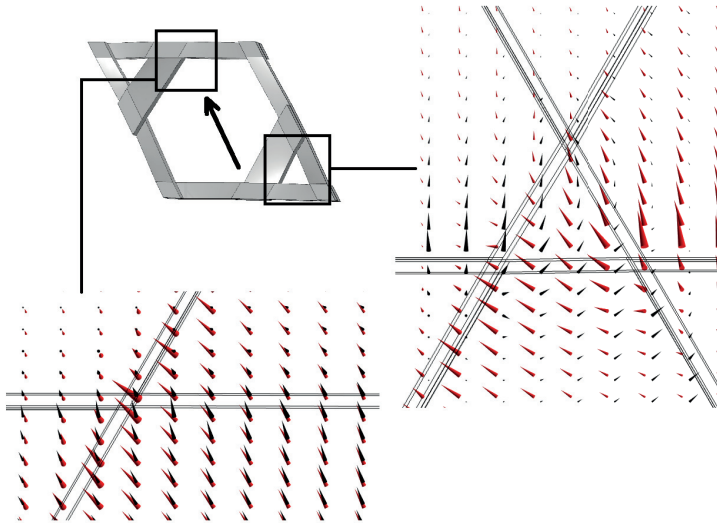


Figure 4.7: Same as Figure 4.6, but with a different polarisation of the excitation.

4.6 Theoretical discussion

A problem with the found symmetry in the slab is that the boundary conditions very much depend on the polarisation of the incident wave. However, the aim of this project is to investigate the reflection properties of the weave and therefore it is only necessary to compute a scattering matrix from two polarisations orthogonal to each other, any other polarisation could then be expressed as a linear combination of those two. Furthermore, in Section 4.4 it was shown that it is a good approximation to consider the weave to be isotropic and therefore one incident polarisation should be sufficient.

4.7 Summary

In this section we have studied the symmetries of the weave and how these can be taken into account in the modelling. The conclusions can be summarised as:

- The infinite slab weave can be constructed by the element presented in Figure 4.8, by two parallel PEC boundaries and orthogonally thereto two parallel PMC boundaries, which follows the orientation of the excitation polarisation.
- For the fine structure weave, the smallest possible representation is the unit cell, see Figure 1.3a.
- It is enough to only consider one incident polarisation.



Figure 4.8: Smallest possible slab element which can correctly represent the entire weave electromagnetically.

5

Parameter sweeps of the slab model

5.1 Introduction

To investigate the electromagnetic performance of the weave and how it is affected by different parameters, a parameter study was conducted. The study was done in numerical simulation programs.

5.2 Simulation model

In order to evaluate the reflection of the weave the slab model is used and the derived symmetries for the slab model from Chapter 4 are implemented. The full wave problem is then computed in the frequency domain for the slab within the frequency range of 10-30 GHz. The implemented computational volume is presented in Figure 5.1. For an explanation of all the used parameter definitions, see Section 1.2.

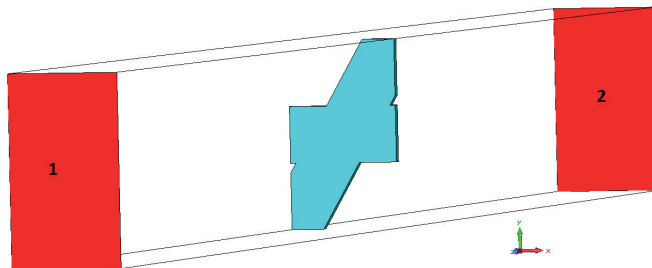


Figure 5.1: The test arrangement of the slab in CST. The volume is excited by a source from port 1 (red) with a polarisation that fits the PEC and PMC boundary conditions. The distance port to port is 20 mm.

5.3 Results

5.3.1 Validation of symmetries and consistency in result from CST and Comsol

To validate that the found symmetry for the slab model is correct, the S_{11} parameter for both the unit cell and the smallest symmetry element was computed and compared in CST and Comsol. The result of this study is plotted in Figure 5.2 and the difference between the two cases is plotted in Figure 5.3. Due to the difference in geometry, it is expected that the discretisation of the two cases should be different, which could be a source of error. In Figure 5.3 one can see that the difference is of the magnitude of 10^{-5} dB, which lies within the numerical error of the computing program. Thus it can be concluded that the found symmetry is valid and it will be used in the following results.

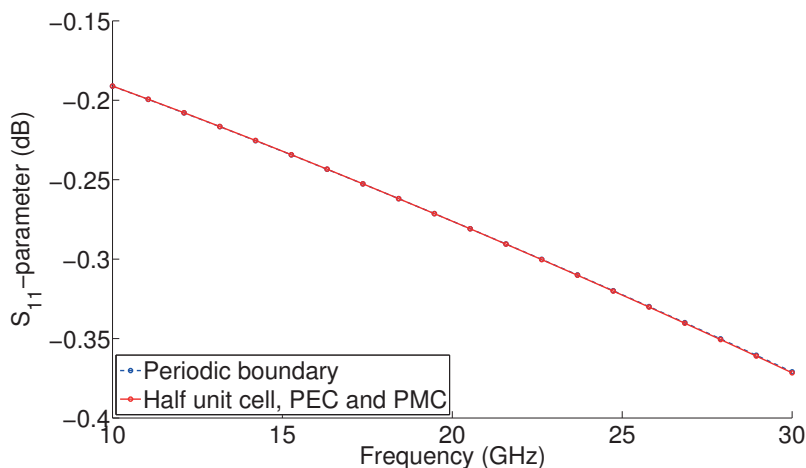


Figure 5.2: S_{11} parameters as function of frequency for the unit cell with periodic boundary conditions (blue) and for the half sized mirror symmetry with PEC/PMC boundaries. The parameters are $a = 1$ mm, $b/a = 0.7$, $\sigma = 10^4$ S/m, $t = 80$ μm . The result was computed in Comsol.

As a further check of correctness of the result, a comparison of the result computed in CST and Comsol for the symmetric element of the slab was performed. The computed reflection parameter for varying thickness is plotted in Figure 5.4.

The found result does not appear to be as consistent as it was for the symmetry/unit cell check (Figure 5.2), but all the results lie within the range of the numerical accuracy of the program. The found differences should serve as a reminder of the actual accuracy of the computed result.

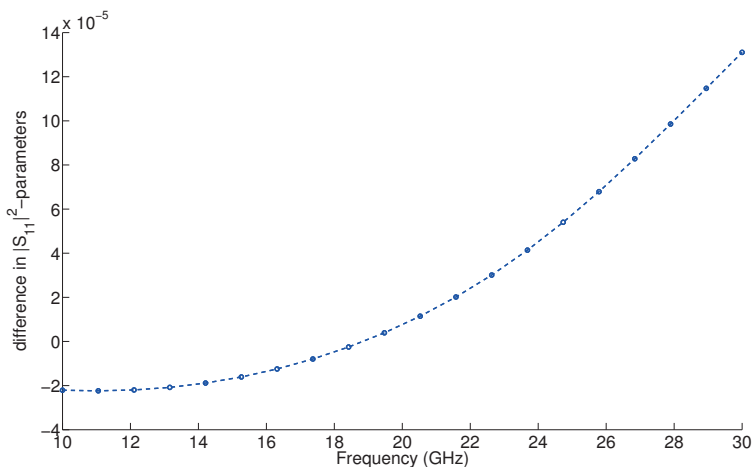


Figure 5.3: Difference in the S_{11} parameters (in Figure 5.2) as function of frequency for the unit cell with periodic boundary conditions and for the half sized mirror symmetry with PEC/PMC boundaries. The parameters are $a = 1$ mm, $b/a = 0.7$, $\sigma = 10^4$ S/m, $t = 80$ μm . The result was computed in Comsol.

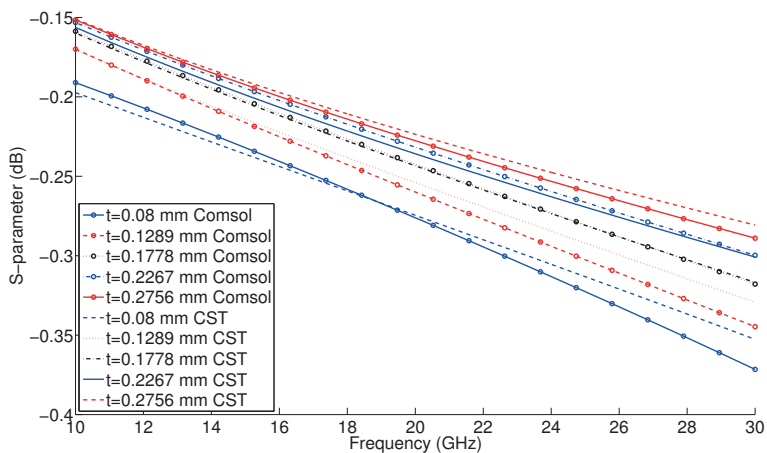


Figure 5.4: Comparison of the result of the computed S_{11} parameters for different slab thickness for CST and Comsol respectively. The other parameters are $a = 1$ mm, $b/a = 0.7$, $\sigma = 10^4$ S/m. The result was obtained from the symmetry model with PEC and PMC boundaries.

5.3.2 Parametric sweep

In Figure 5.5-5.8 are the computed reflection coefficients for a parametric sweep of the slab conductivity, thickness, unit cell to hole size ratio and unit cell size in CST

presented. In Figure 5.5 the reflection coefficient of the slab is plotted as a function of the frequency at different slab conductivities. It is clear that the slab conductivity has a major impact on the reflection coefficient and that a conductivity of 10^4 S/m is not sufficient. For a higher conductivity of 10^5 to $1.5 \cdot 10^5$ S/m the reflection coefficient reaches the demanded design requirement.

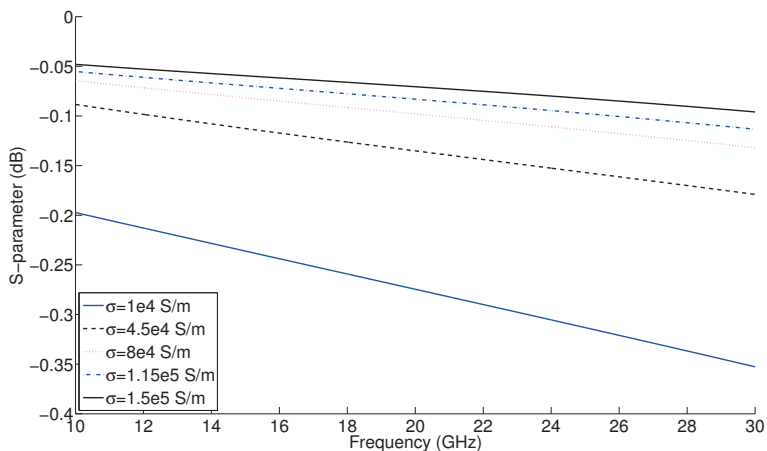


Figure 5.5: S_{11} parameters as function of frequency at different conductivities in the slab for the symmetry model with PEC and PMC boundaries. The other parameters are $a = 1$ mm, $b/a = 0.7$, $t = 80 \mu\text{m}$. The result was computed in CST.

Similarly, in Figure 5.6 the reflection coefficient of the slab is plotted as a function of the frequency for different slab thicknesses. The thickness has not as big of an impact as the conductivity has, but it is clear that a thicker slab gives a higher reflection.

To find how the weave shape affects the reflection coefficient, the ratio of the unit cell size and its hole size is swept. From Figure 5.7 it is obvious that a smaller hole gives a higher reflection coefficient. That is that $b/a = 2/3$ is the optimal electromagnetic design.

The final parameter that is of interest in the weave is how the unit cell size affects the reflection coefficient. In Figure 5.8 the reflection coefficient is plotted as a function of frequency at different unit cell sizes ($2a$). As in the b/a -ratio plot above, one can yet again conclude that a smaller hole, that is smaller unit cell size in this case, gives a higher reflection coefficient.

5.3.3 Incidence angle sweep

A further interesting and important property of the weave is how the reflection coefficient depends on the relative angle of the incident wave and the weave. To simulate this a CAD model of the unit cell in the fine structure weave including details as insulation was imported to CST. Results from three of these sweeps are presented in Figure 5.9, 5.10 and 5.11.

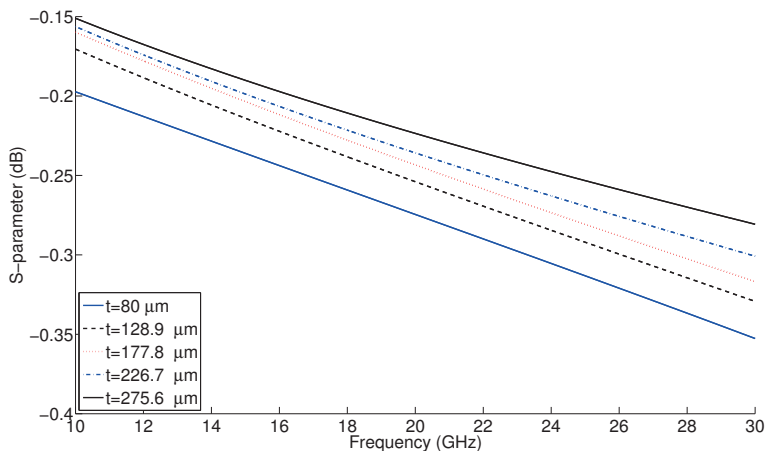


Figure 5.6: S_{11} parameters as function of frequency at different thickness of the slab for the symmetry model with PEC and PMC boundaries. The other parameters are $a = 1$ mm, $b/a = 0.7$, $\sigma = 10^4$ S/m. The result was computed in CST.

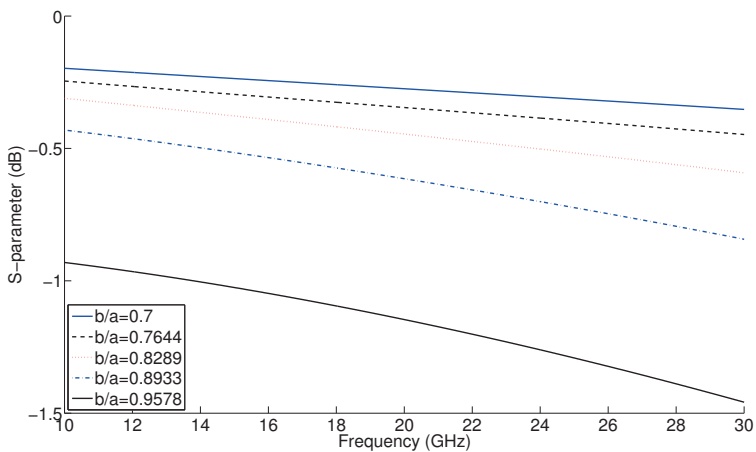


Figure 5.7: S_{11} parameters as function of frequency at different b/a ratios in the slab for the symmetry model with PEC and PMC boundaries. The other parameters are $a = 1$ mm, $\sigma = 10^4$ S/m, $t = 80$ μ m. The result was computed in CST.

From the figures it can be concluded that the reflection coefficient does not depend at all on the azimuthal angle of the wave relative the weave, but very much on the elevation angle to the weave. It can also be concluded that there is a difference in how the TE and TM polarisation behaves depending on incident θ angle. The reflection

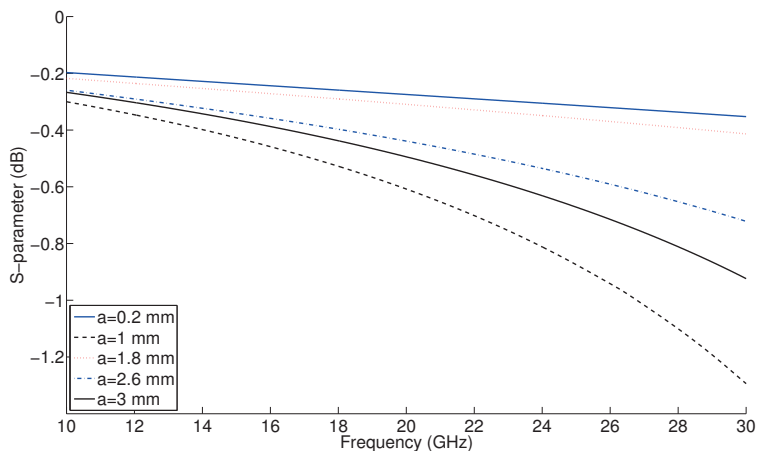


Figure 5.8: S_{11} parameters as function of frequency at different sizes of the unit cell ($2a$) of the slab for the symmetry model with PEC and PMC boundaries. The other parameters are $b/a = 0.7$, $\sigma = 10^4$ S/m, $t = 80$ μm . The result was computed in CST.

of the TE-polarisation increases and the reflection of the TM-polarisation decreases as the propagation direction of the wave becomes parallel to the weave, see Figure 5.11.

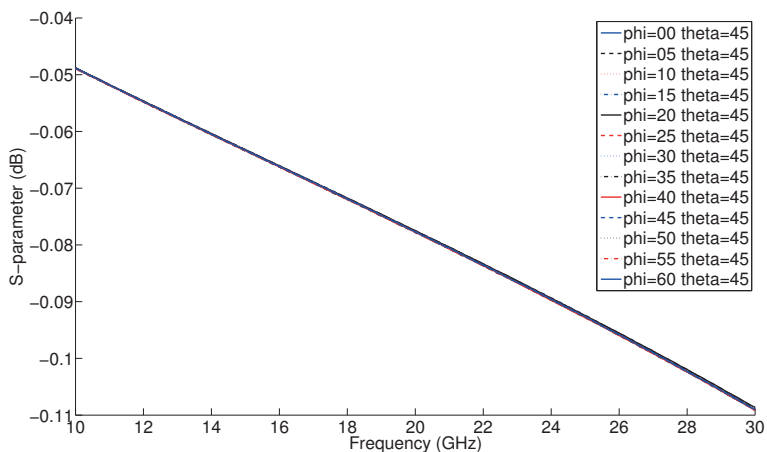


Figure 5.9: TE S_{11} parameters as function of frequency at different incidence angles. In this plot is the angle of the normal to the weave (θ) kept constant at $\pi/4$ and the azimuthal angle (ϕ) is swept from 0 to $\pi/3$. The parameters are $a = 1$ mm, $b/a = 0.7$, $\sigma = 10^5$ S/m, $t = 240$ μm . The results were computed for the fine structure weave in CST.

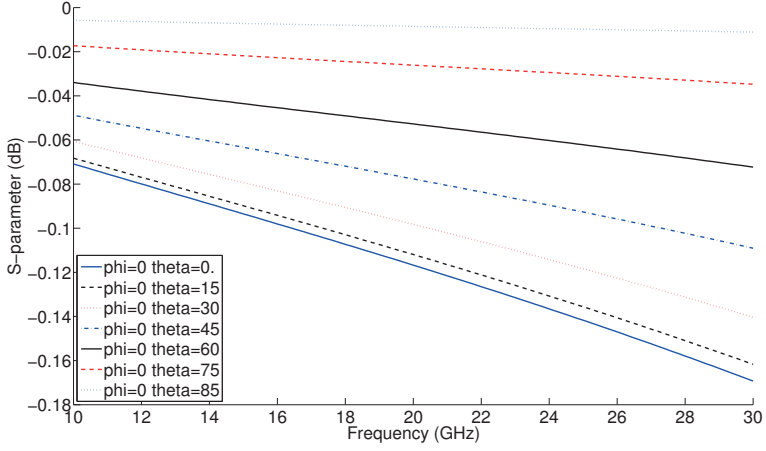


Figure 5.10: TE S_{11} parameters as function of frequency at different incidence angles. In this plot is the angle of the normal to the weave (θ) is swept from 0 to 85 degrees and the azimuthal angle (ϕ) kept constant to 0 degrees. The parameters are $a = 1$ mm, $b/a = 0.7$, $\sigma = 10^5$ S/m, $t = 240$ μm . The results were computed for the fine structure weave in CST.

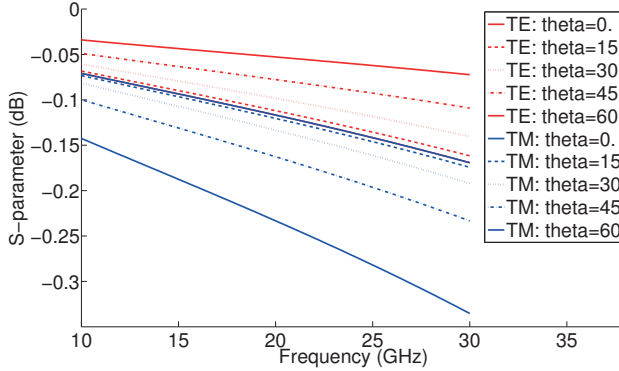


Figure 5.11: The S_{11} parameter as function of frequency at different incidence angles for the TE polarisation and TM polarisation for the fine structure model. The parameters are $a = 1$ mm, $b/a = 0.7$, $\sigma = 10^5$ S/m, $t = 240$ μm . The results were computed for the fine structure weave in CST.

5.3.4 Further observations

Running the parameter sweep raises the question; How well would the weave perform if one uses the found realistic optimal parameters. In Figure 5.12 the reflection coefficient as function of the frequency is plotted for these optimal parameter values and compared

to the presented weave. It can then be concluded that it is possible to reach the electromagnetic design requirement with only one carbon fibre weave layer. However, due to the appearance of the weave there is a manufacturing limit of how small one can make the unit cell (a) that depends on the properties and dimensions of the weave strings. A smaller unit cell might also not be beneficial for the acoustical behaviour of the weave.

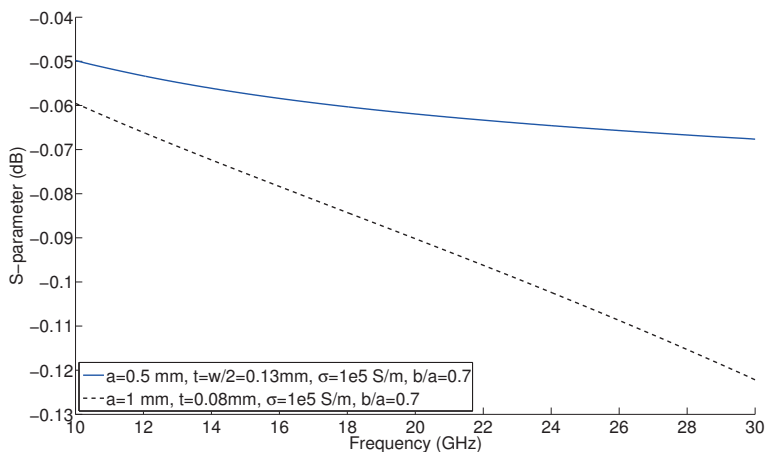


Figure 5.12: A comparison of the optimal weave design ($a = 0.5$ mm (as small as possible), $b/a = 0.7$, $\sigma = 10^5$ S/m, $t = 130$ μm ($\approx w/2$)) and the given design ($a = 1$ mm, $b/a = 0.7$, $\sigma = 10^5$ S/m, $t = 80$ μm). Both results were computed in CST.

5.3.5 Power losses

For the given weave, it is of interest to understand what the source of power loss is in order to know where to focus on improving the design. The theoretical derived transmission loss and conductivity loss is therefore plotted in Figure 5.13. It can then be concluded that the major source of power loss is the conductivity loss.

Theory

A method to estimate the conductivity loss in the weave is to compare the feeding power sent into the test volume with the power leaving the system at the ports, see (5.1) [6]. The difference must then be due to power loss within the weave or numerical errors.

$$\Delta P_{\text{cond}} = 1 - |S_{11}|^2 - |S_{21}|^2 - |S_{31}|^2 - |S_{41}|^2 \quad (5.1)$$

By a similar reasoning the relative transmitted power is the power leaving at the ports 3 and 4, see (5.2).

$$\Delta P_{\text{trans}} = |S_{31}|^2 + |S_{41}|^2 \quad (5.2)$$

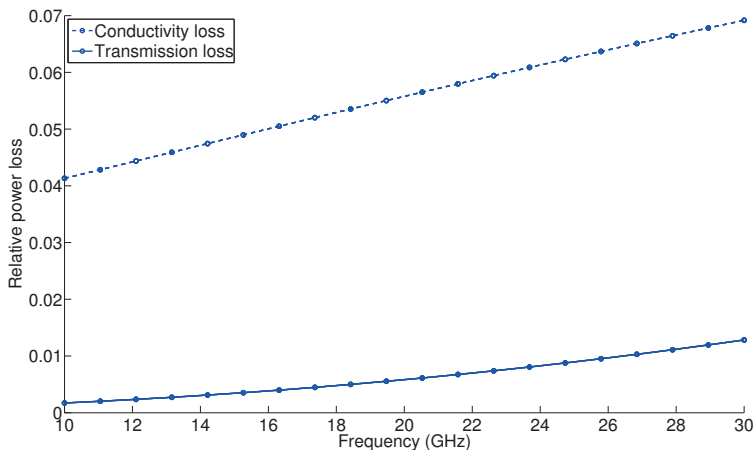


Figure 5.13: Relative power losses in the weave due to transmission losses and conductivity losses. The parameters are $a = 1$ mm, $b/a = 0.7$, $\sigma = 10^4$ S/m, $t = 80$ μm . The results were computed in Comsol.

5.4 Summary

The smallest found symmetry for the slab model could be validated. It could also be concluded that the reflection coefficient is independent on the azimuthal angle (ϕ), but is highly dependent on the normal incident angle to the weave (θ). Furthermore, the reflection coefficient differs for the TE and TM polarisations at different elevation incidence angles (θ).

Changing the dimensions of the weave greatly impacts the reflection coefficient of the weave. A thicker weave gives a slightly higher reflection coefficient. However, the main difference is due to how densely the unit cell is covered. The highest reflection coefficient is obtained by a hole side to unit cell side ratio of $b/a=0.7$. Similarly, a smaller unit cell size gives a higher reflection coefficient.

Another parameter that has a major impact on the reflection is the conductivity. A higher conductivity gives a higher reflection coefficient. The main energy loss with a conductivity of $\sigma = 10^4$ S/m in the weave is the conductivity loss, implying that a high carbon fibre conductivity is preferable.

It is possible to obtain the design requirement for the whole frequency range by a plain single tri-axial carbon fibre weave by only modifying the dimensions of the unit cell. One example would be $a = 0.5$ mm, $b/a = 0.7$, $\sigma = 10^5$ S/m, $t = 130$ μm , see Figure 5.12.

To summarise the result of the parametric sweep some reasonable guiding values are presented in Table 5.1. These values combined are not sufficient to reach the designing requirement, but should be tweaked in accordance to the inequalities.

Parameter name	Value
σ	$> 10^5$ S/m
b/a	0.7
a	< 1 mm
t	> 80 μm

Table 5.1: Summary of the parametric sweep. Note that the conductivity and the b/a ratio is of most importance. Note that the inequalities are guidelines to how the parameters should be tweaked and that $a = 1$ mm, $b/a = 0.7$, $\sigma = 10^5$ S/m, $t = 80$ μm does not fulfil the design requirement, see Figure 5.1.

6

Coating

6.1 Introduction

A method that is frequently used to increase the reflection of a structure is to coat it with a highly conductive material such as a metal paint. The idea as such is not very complicated but the manufacturing process is rather expensive. Another issue with coating is the PIM effect that is very likely to be problematic when adding a coating layer, see Section 2.4.5.

For these reasons coating is not a very desirable performance improvement technique, but it is still interesting to understand how much the performance of the weave increases by metal coating in order to compare it with other available methods.

6.2 Method and results

The method used here is similar to that in Chapter 5. The smallest slab symmetry unit cell was implemented in CST with the difference that the surfaces parallel to the weave were set as PEC surfaces. An example of this is shown in Figure 6.1. The reflection coefficient was then computed from the full wave model in CST.

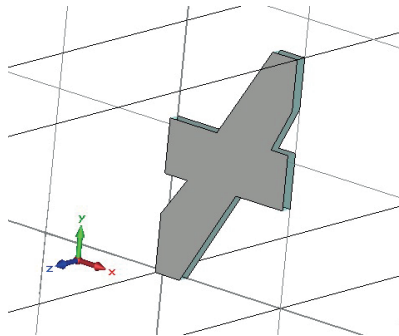


Figure 6.1: This picture describes what the CST implemented coating model looks like. In this case is both the front side and back side of the slab coated with a PEC surface. In-between there is a homogeneous carbon fibre material.

In Figure 6.2 the reflection coefficient for the double respective single coated weave is plotted in the frequency range of 10-30 GHz. From the plot one can see that just using coating at one side is enough to reach the design requirement of -0.1 dB. By coating both sides of the weave the performance increases slightly more.

Since the project is a co-optimisation problem it is interesting to understand how much one can increase the hole size and still reach the design requirement by coating. Therefore a parameter sweep was done and presented in Figure 6.3. From the figure one can conclude that the ratio $b/a = 0.79357$ is enough to reach the design requirement of -0.1 dB when the weave is coated by a metal sheet at both sides.

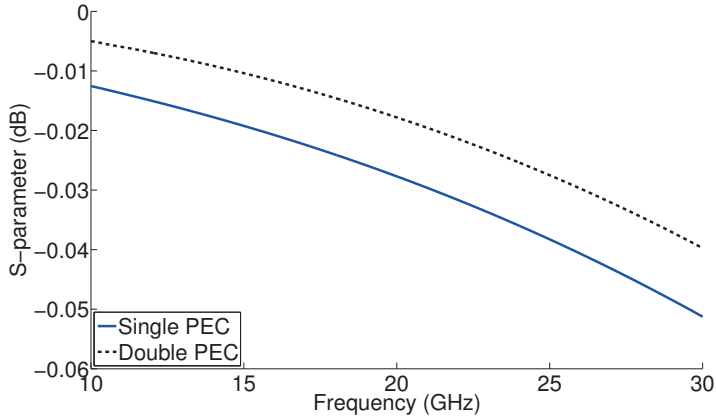


Figure 6.2: S_{11} parameters as function of frequency as a comparison of the performance when the slab only is coated on the front side (single PEC layer) and both the front and back side (double). The other parameters of the slab was $a = 1$ mm, $b/a = 0.7$, $t = 80$ μm , $\sigma = 10^5$ S/m. The results were computed in CST.

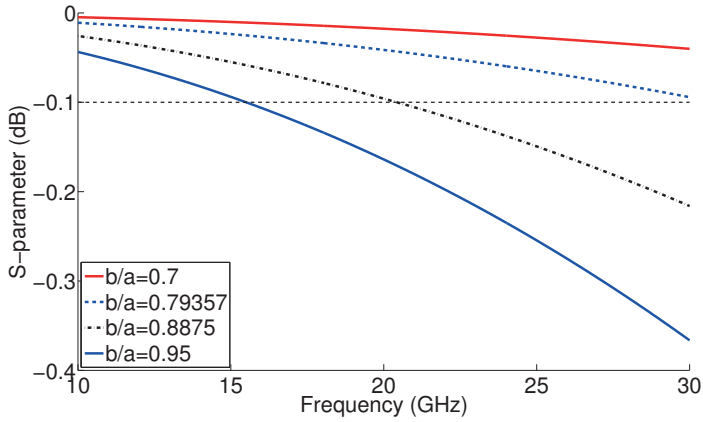


Figure 6.3: S_{11} parameters as function of frequency for different b/a ratios in the slab with double PEC coating. The other parameters of the slab are $a = 1$ mm, $t = 80$ μm , $\sigma = 10^5$ S/m. The results were computed in CST. The black dotted line is the design requirement of -0.1 dB.

6.3 Summary

Coating is an easy method to obtain a higher conductivity and it is even possible to change the dimension of the unit cell slightly and still meet the design requirement. However, the simulations do not consider the impurities that occur during the manufacturing process that give rise to the undesirable PIM effect. For this reason coating is not a good performance enhancing method in this case.

7

Dual weave arrangements

7.1 Introduction

An intuitive way to improve the reflection performance of the weave is to add an additional weave layer. Introducing this new geometry gives rise to new phenomena and behaviours that must be investigated.

One example of such a phenomena is the rise of moiré patterns. A moiré pattern is a pattern that appears when two sets of lines, where one of the sets is rotated slightly to the other sets, are added on top of each other. An example of this is presented in Figure 7.1. Another example of a moiré pattern from the triaxial weave is presented in Figure 7.2. The name "moiré" originates from a french word for a textile [4].

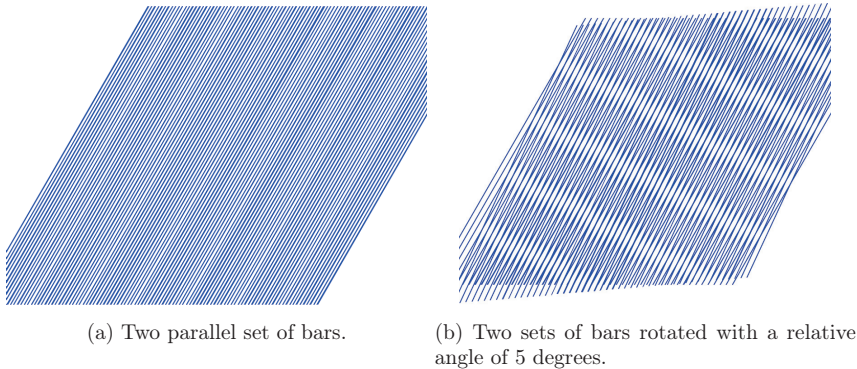
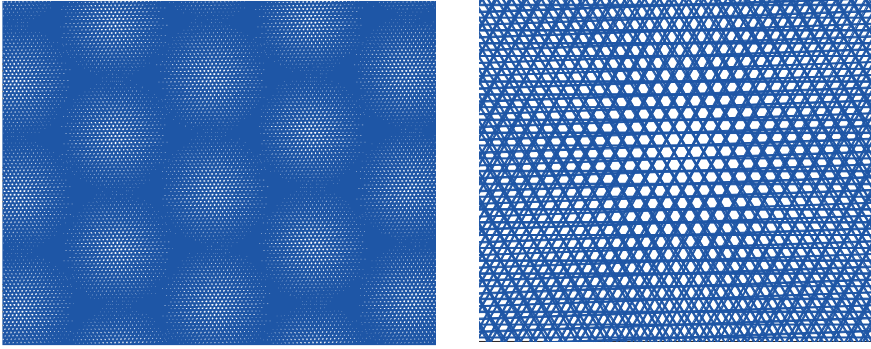


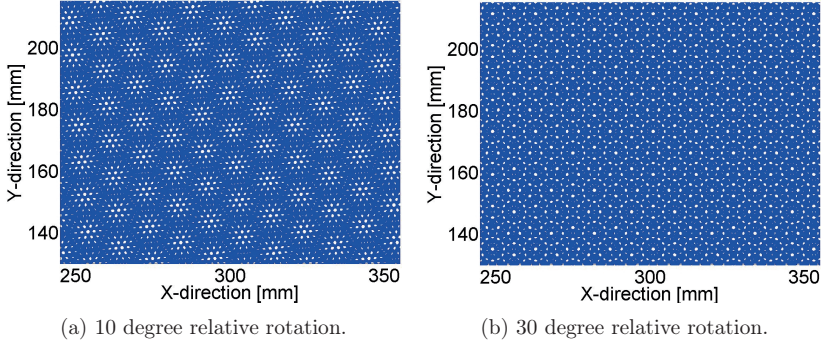
Figure 7.1: An illustration of the rise of moiré patterns with parallel bars.



(a) At a macroscopic level

(b) Zoomed in at a sparse area.

Figure 7.2: The moiré pattern for the double weave with a 2 degree relative rotation when $a/b=0.7$ and $a=1$ mm.



(a) 10 degree relative rotation.

(b) 30 degree relative rotation.

Figure 7.3: The moiré pattern at a relative rotation of 10 respectively 30 degree in the case where $a=1$ mm and $b/a=0.7$.

7.2 An analytical and numerical approach to understanding the moiré pattern

A mathematical investigation was performed to better understand the behaviour of the dual weave and its moiré pattern. The study is aimed to describe the area covered by the dual weave as a function of the relative rotation degree and investigate the existence of reoccurring patterns and its periodicity. It was found that the relative

area covered by an infinite dual weave can be calculated for rotation angles where a periodicity exists, and there is periodicity when the cosine of the relative rotation angle is a rational number. This fact gave a surprisingly complicated behaviour of the periodicity.

7.2.1 Derivation of a method

Starting from the hypothesis that a dual weave with a relative rotation has a periodicity, that is that the mid points of the unit cells in each weave layer coincide and yet again coincide with the periodicity, see Figure 7.4. It was discovered that this is not always possible and is only valid for angles φ (see Figure 7.5) which fulfil $\cos(\varphi) \in \mathbb{Q}$, where \mathbb{Q} denotes the set of rational numbers. The infinite dual weave can then be represented by this finite group of elements and the hole area to the total area ratio can be calculated by summing up the intersection of the holes within the group of elements.

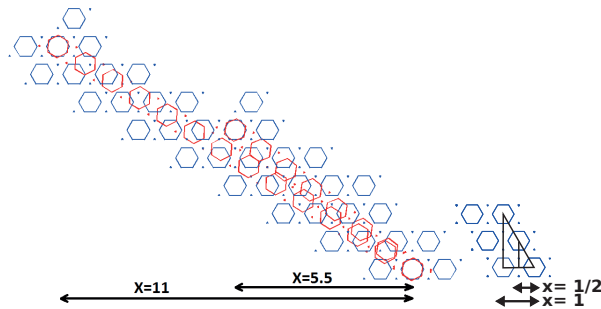


Figure 7.4: The holes of two weaves on top of each other for two different cases of a relative rotation of 32.2° (corresponding to $x/y = 11/13$ in (7.1)) and relative rotation of 38.2° (corresponding to $x/y = 5.5/7$ in (7.1)) Note that the case when $x = 5.5$ corresponds to the right triangle in Figure 7.5.

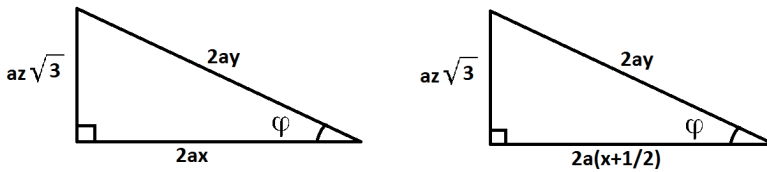


Figure 7.5: Triangles representing the two relatively rotated weaves and the constraint that 3 integer numbers (x, y and z) of elements with the side length $2a$ must represent the triangle. The example of $x = 11$ in Figure 7.4 corresponds to the left triangle in this figure. Similarly the right triangle represent the case of $x = 5.5$ correctly.

Consider Figure 7.5. One then finds the constraints (7.1) and (7.2) or (7.3) and (7.4) depending on which case in Figure 7.5 is considered

$$\cos(\varphi) = \frac{2ax}{2ay} = \frac{x}{y}, \quad y, x \in \mathbb{Z} \quad (7.1)$$

$$z = 2\sqrt{\frac{y^2 - x^2}{3}}, \quad z \in \mathbb{Z} \quad (7.2)$$

$$\cos(\varphi) = \frac{2a(x+\frac{1}{2})}{2ay} = \frac{x+\frac{1}{2}}{y}, \quad y, x \in \mathbb{Z} \quad (7.3)$$

$$z = 2\sqrt{\frac{y^2 - (x+\frac{1}{2})^2}{3}}, \quad z \in \mathbb{Z} \quad (7.4)$$

where \mathbb{Z} denotes the set of integers. This method requires that $\cos(\varphi) \in \mathbb{Q}$ in (7.1) or (7.3). For ratios that are irrational the pattern is quasi periodic. An approximative periodicity can be found for these cases by e.g. expanding the irrational number as a finite continued fraction. The magnitude of these found rational numbers then corresponds to the periodicity. These periodicities can be very big and it can thus be very computationally demanding to use these periodicities to model the dual weave.

7.2.2 Periodicity

The results presented in this section are all computed by defining a set of points in accordance to (7.1), (7.2), (7.3), and (7.4), an upper bound and the first quadrant of the xy-plane. See Figure 7.6. For each point the angle φ in (7.1) or (7.3) is then computed. This gives the periodicity in number of elements along the directions of the edges in the triangles of Figure 7.5. The periodicity in the x- and y-direction for all the points in the set are plotted in Figure 7.8. Note that the points are "symmetric" around 30° and periodic with 60° . This is expected due to the single weave being rotationally symmetric with 60° and since rotating the weave plus one degree should give a similar macroscopic pattern as rotating it minus one degree. Thus it must be symmetric around 30° and 60° .

Finally in Figure 7.7 the minimum found periodicity for each rotation is plotted. This plot is not very easy to intuitively understand. To start with one must understand that the domain of the periodicity function is not continuous. That is that the ratio in (7.1) must be rational. To get a good resolution of the graph a rather high discretion is done of $\sim 23.4 \cdot 10^3$ points originating from $3.6 \cdot 10^6$ points which are filtered by (7.1), (7.2), (7.3), and (7.4), see Figure 7.6.

An interesting consequence of the constraint in (7.1) and (7.2) is that angles that give rise to an irrational ratio do not have a macroscopic periodicity in the dual weave. By approximating the number with continuous fraction the periodicity will be a high number which increases as the accuracy of the approximation increases. In the limit the periodicity lies at the infinity and would be visualised in Figure 7.7 as a Dirac delta function. Two rather interesting angles that give rise to irrational numbers are 30° and 45° .

This numerical approach and the problem with irrational ratios are the reasons for the odd shape of Figure 7.7. A further explanation of its appearance can be found in Section 7.2.2

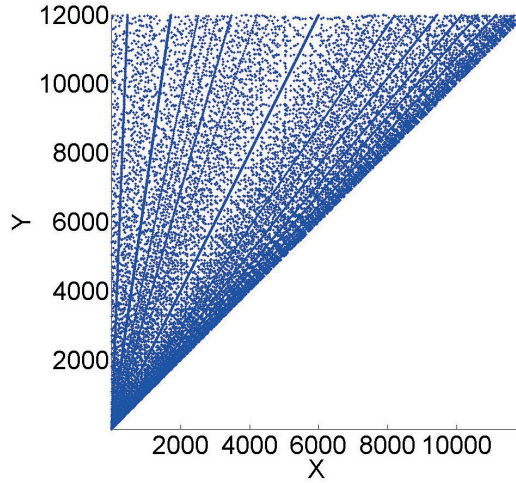


Figure 7.6: Computational domain of the discrete points which fulfil the properties of (7.1) and (7.2).

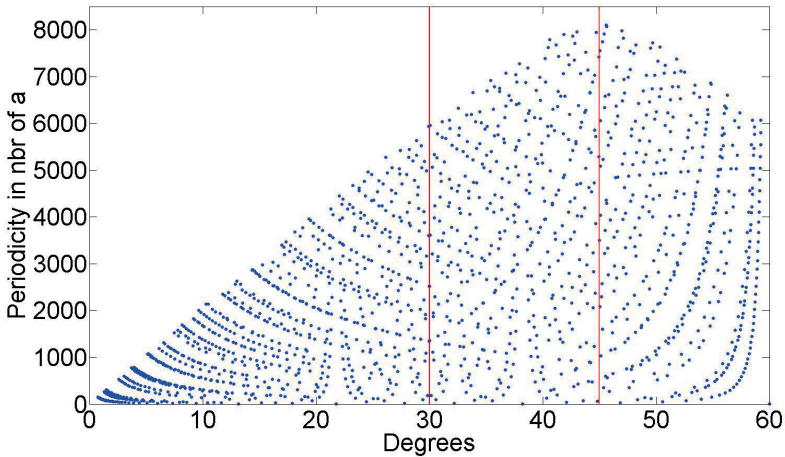


Figure 7.7: The minimum periodicity ($\min(x,y,z)$) in the dual weave as a function of the relative rotational angle φ . The reason why the graph does not appear to be symmetric around 30° and has a uniform distribution is due to a finite number approximation of the irrational ratios in (7.1) or (7.3) and that φ is only in the interval of $]0^\circ, 90^\circ[$ instead of $]0^\circ, 360^\circ[$. The red lines mark 30° and 45° . For a further discussion of the appearance see Section 7.2.2.

Explanation of the appearance in Figure 7.7

To explain the peak at 45° in Figure 7.7, consider Figure 7.5. Let us first notice that y periodicity will never be present in Figure 7.7 due to the fact that the

hypotenuse is always longer than its cathetus. Furthermore, it is then obvious according to Pythagoras theorem that:

$$\begin{aligned} z\sqrt{3} &> 2x && \text{when } \varphi > 45^\circ \\ z\sqrt{3} &< 2x && \text{when } \varphi < 45^\circ \end{aligned} \quad (7.5)$$

In Figure 7.6 one can do the following observation. Along the boundaries $x=0$ and $y=x$ the ratio in (7.1) is:

$$\begin{aligned} \frac{x}{y} \rightarrow 0 &\implies \varphi = 90^\circ \\ \frac{x}{y} \rightarrow 1 &\implies \varphi = 0^\circ \end{aligned} \quad (7.6)$$

This means that for $\varphi \approx 0$ the x periodicity will be close to the maximum corresponding discrete value. Similarly the x periodicity will decrease as $\varphi \rightarrow 90^\circ$. However, one can also do the following observations:

$$\begin{aligned} x \rightarrow 0 &\implies z\sqrt{3} \rightarrow 2y \\ x \rightarrow y &\implies z \rightarrow 0 \end{aligned} \quad (7.7)$$

The z periodicity has a similar behaviour to the x one but opposing. The minimum periodicity of the union of these functions will then be bell shaped with a peak at 45° .

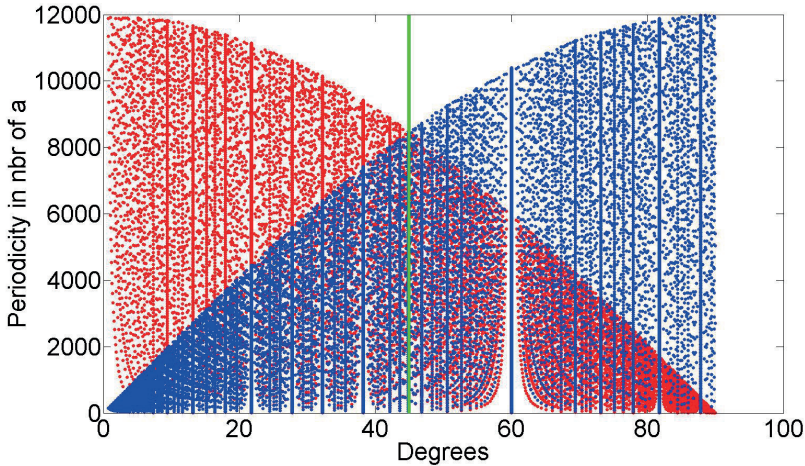


Figure 7.8: All possible periodicities in the x (red) and z (blue) direction as function of φ in degrees with a certain discretion in accordance to Figure 7.6. Note the appearance of the bell shape seen in Figure 7.7. The green line marks 45° .

7.2.3 Relative hole area

By a similar method to the periodicity investigation, the total hole area in the dual weave was investigated. Since a row of elements was constructed for each φ and its hole intersection computed in accordance to Figure 7.4, the computational load quickly

increases. This limits the possible discretion of the relative angle φ to only ~ 50 values. The results are presented in Figure 7.9 and 7.10.

The starting hypothesis of this investigation was that there is a minimum hole area at 30 degrees. This could not be proven due to the fact that the ratio in (7.1) for 30 degrees is irrational. However by only looking in Figure 7.10 it still seems plausible that there is a minimum at 30 degrees. Either way one can conclude that there is a significant difference in hole coverage at a small relative rotation in the dual weave.

An interesting property of the dual weave that was found is that the hole ratio appears to be the relative hole area ratio of the single weave squared. In Figure 7.9 it corresponds to $0.37^2 = 0.1369$.

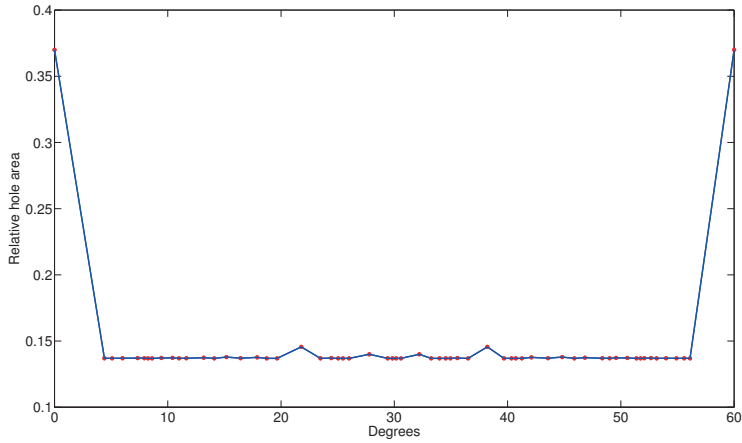


Figure 7.9: The relative hole area calculated in some points from 0 to 60 degrees.

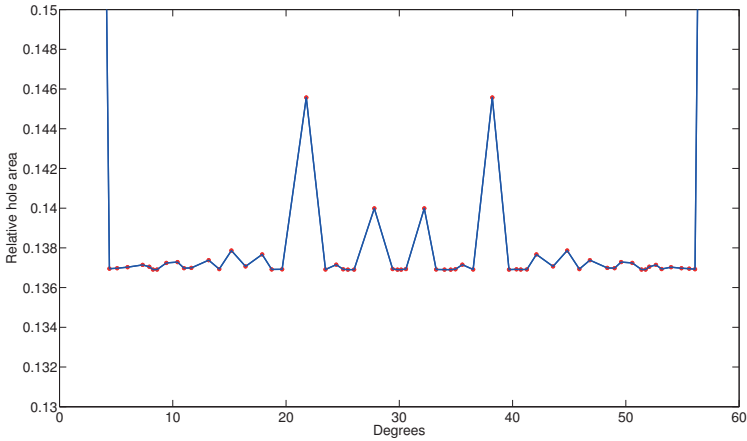


Figure 7.10: Same as Figure 7.9 but slightly zoomed in. Note that the graph appears to be symmetric around 30° , which is expected since rotating \pm the same number of degrees starting from non rotated should give a similar macroscopic pattern (possibly mirrored).

7.3 Approximation of the reflection coefficient at a macroscopic scale

There are some difficulties when one numerically tries to represent the relative translation and rotation of the double weave. The most efficient and general method to represent the weave in this case is to use periodic boundaries. Some programs have the ability to automatically find and replicate elements of the structure to fit its periodic boundaries. One constrain in that context is that the periodicity is the same in the different elements. However if one rotates one of the elements relative to the other the periodicity is lost. It is then not possible to numerically compute the reflection coefficient of two unit cells that are rotated to each other, which is necessary to investigate the moiré pattern of the dual weave.

This is the reason why an approximation is introduced. This is how the approximation is done:

- Use a software to compute full wave solutions at a fixed frequency and sweep the non-rotated relative unit cell orientation of the dual weave in the x and y directions.
- Compute the mid points of the holes for the respective weaves.
- For every mid point in the top layer; find the closest located midpoint of the second layer.
- Map the computed swept result with the macro pattern based on a match of closest mid point.

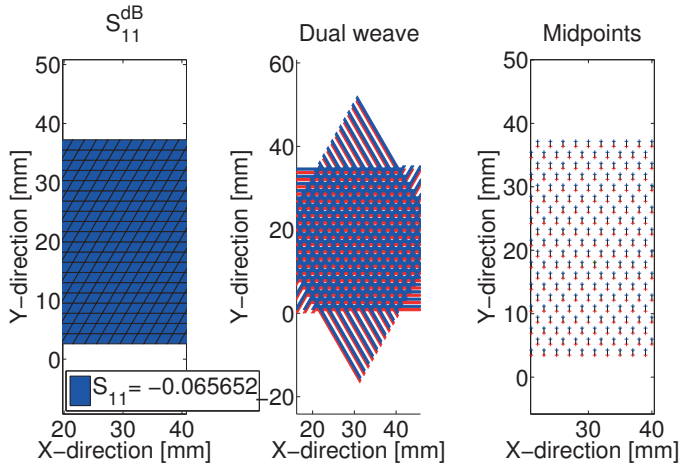


Figure 7.11: Example plots, which are meant to explain the moiré-mapping-approximation method. The plots are automatically generated from CST data. In this case the weaves are relatively translated 0.8 mm in y direction.

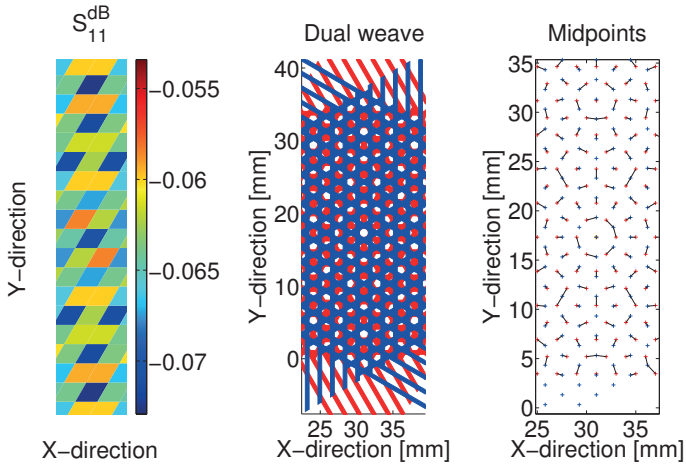


Figure 7.12: Example plots, which are meant to explain the moiré-mapping-approximation method. The plots are automatically generated from CST data. In this case the weaves are relatively rotated by 30 degrees.

7.3.1 Relative translation

In Figure 7.13-7.17 are some results presented for the case when the weaves are relatively translated in the x - respective y -direction. This was the only case where the results could be numerically computed exactly.

Some reflection coefficients are plotted in Figure 7.13 and 7.15 as a function of the frequency. Notice that by adding one weave, without translating it, is enough to reach the required design parameter. Compare this to the result in 5.5. In Figure 7.14 and 7.16 the macroscopic pattern at x and y translations are drawn and the reflection coefficients at the frequency of 20.12 GHz are computed.

In Figure 7.17 the relative phase shift is plotted. That is how much the phase changed additionally to the 180° that normally occur at reflection from a PEC surface. From Figure 7.17 can one see that the interval of phase change is $[-0.53, 0.75]$ degrees.

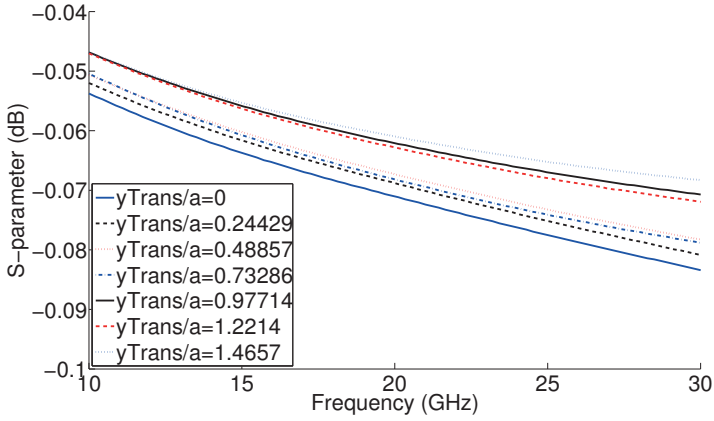


Figure 7.13: S_{11} parameters as function of frequency at different translation in the y-direction in the dual weave with periodic boundary conditions in the slab model. The other parameters are $a = 1$ mm, $b/a=0.7$, $\sigma = 10^5$ S/m, $t = 80$ μm , distance between the slabs is 0.2 mm. The result was computed in CST.

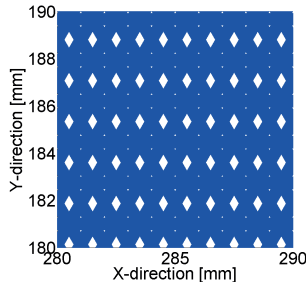


Figure 7.14: Macroscopic view of the dual weave. The weave are translated in the y-direction with $a\sqrt{3}$. This results in the same reflection coefficient at every unit cell throughout the whole weave, which at the frequency of 20.12 GHz is -0.059616 dB. Note that this can be computed without an approximation in CST. $a=1$ mm, $b/a=0.7$, $\sigma = 10^5$ S/m and $t = 80$ μm , distance between the slabs is 0.2 mm.

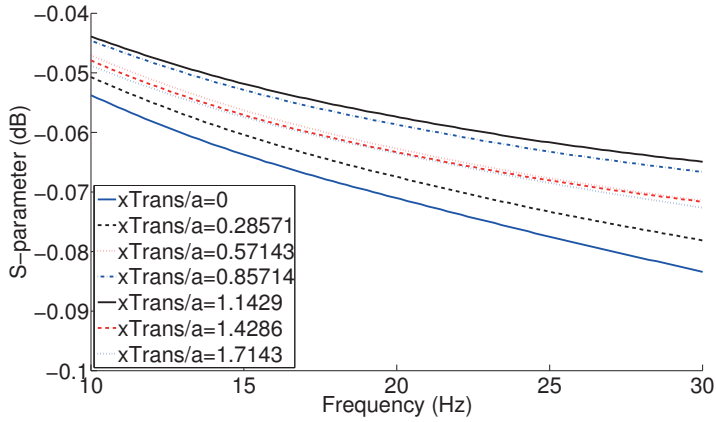


Figure 7.15: S_{11} parameters as function of frequency at different translation in the x -direction in the dual wave with periodic boundary conditions in the slab model. The other parameters are $a = 1$ mm, $b/a=0.7$, $\sigma = 10^5$ S/m, $t = 80$ μm , distance between the slabs is 0.2 mm. The result was computed in CST.

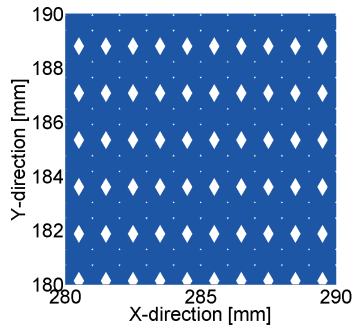


Figure 7.16: Similarly to Figure 7.14. Macroscopic view of the dual wave. The wave are translated in the x -direction with a . This results in the same reflection coefficient at every unit cell throughout the hole wave, which at the frequency of 20.12 GHz is -0.059616 dB. Note that this can be computed without an approximation in CST. $a=1$ mm, $b/a=0.7$, $\sigma = 10^5$ S/m and $t = 80$ μm , distance between the slabs is 0.2 mm.

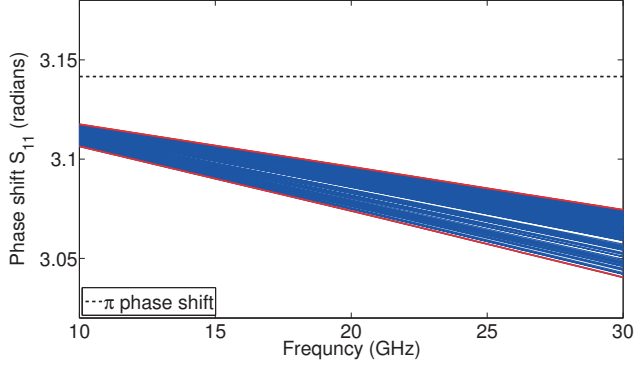


Figure 7.17: The relative phase shift of the S_{11} reflection coefficient as function of the frequency, when the weaves are relative translated with 225 combinations in the interval of $[0, 2a]$ in x-direction and $[0, a\sqrt{3}]$ in the y-direction. The red lines corresponds to the cases when the weaves are relative translated by $[0.571, 1.344] \cdot a$ and $[0.429, 0.489] \cdot a$. The case when there is not any translation lies in the middle in-between the red lines.

7.3.2 Relative rotation

In this section the results obtained by the approximation are introduced in Section 7.3. Note that the resolution of the discretisation is limited by the x- and y-translated result. In this case the moiré pattern is mapped to 225 combinations of x- and y-translated CST results, which lie in the interval of $[0, 2a]$ in the x-direction and $[0, a\sqrt{3}]$ in the y-direction.

Due to this fact the color legend in the plots spans the same values at different relative rotation. Despite this fact the plots display an idea of the macroscopic behaviour in the dual weaves. The reflection coefficient as a function of plane coordinates are presented in Figure 7.18b, 7.20b, 7.22b and 7.24b, correspondingly the relative phase shift presented in Figure 7.19, 7.21, 7.23 and 7.25.

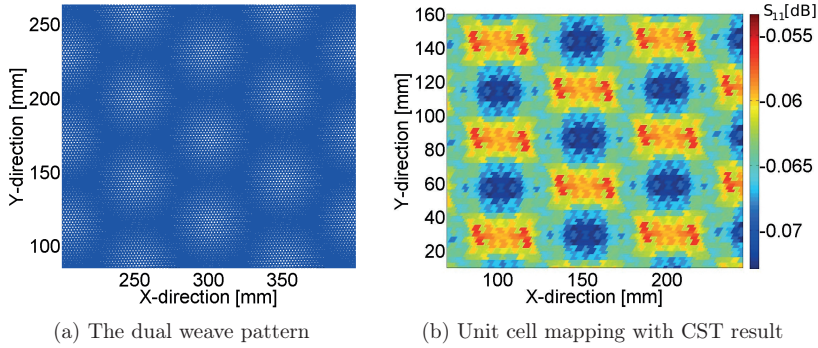


Figure 7.18: Macroscopic view of the dual wave. The weaves are rotated with a relative angle of 2° . (b) is the mapped result of CST and (a), at the frequency of 20.12 GHz. Note that this is an approximation. $a=1$ mm, $b/a=0.7$, $\sigma = 10^5$ S/m and $t = 80$ μm , distance between the slabs is 0.2 mm.

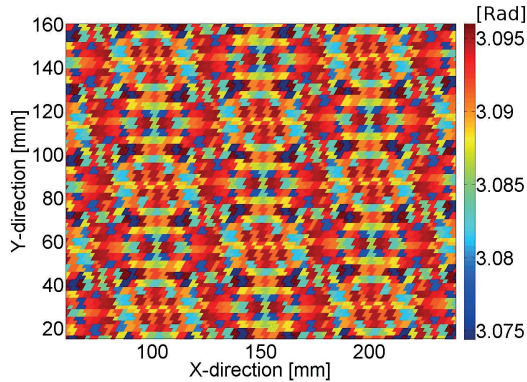


Figure 7.19: Macroscopic view of the dual wave. The weaves are rotated with a relative angle of 2° . It is the mapped result of CST and the geometrical moiré pattern, at the frequency of 20.12 GHz. Note that this is an approximation. $a=1$ mm, $b/a=0.7$, $\sigma = 10^5$ S/m and $t = 80$ μm , distance between the slabs is 0.2 mm.

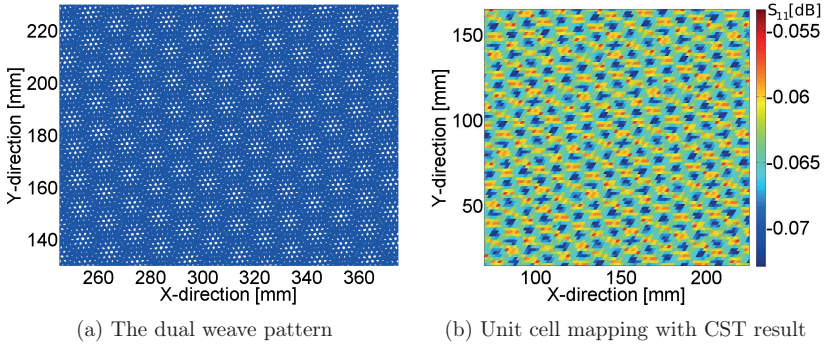


Figure 7.20: Macroscopic view of the dual wave. The weaves are rotated with a relative angle of 10° . (b) is the mapped result of CST and (a), at the frequency of 20.12 GHz. Note that this is an approximation. $a=1$ mm, $b/a=0.7$, $\sigma = 10^5$ S/m and $t = 80$ μm , distance between the slabs is 0.2 mm.

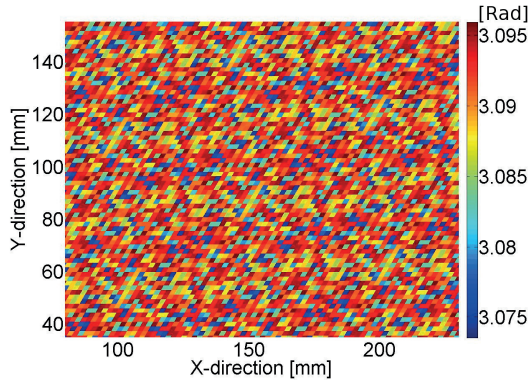


Figure 7.21: Macroscopic view of the dual wave. The weaves are rotated with a relative angle of 10° . It is the mapped result of CST and the geometrical moiré pattern, at the frequency of 20.12 GHz. Note that this is an approximation. $a=1$ mm, $b/a=0.7$, $\sigma = 10^5$ S/m and $t = 80$ μm , distance between the slabs is 0.2 mm.

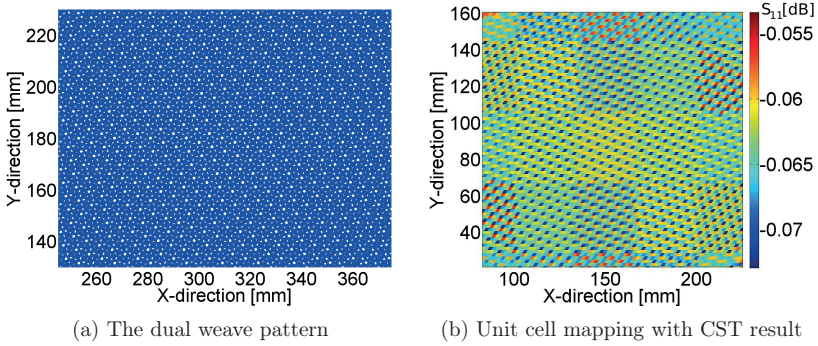


Figure 7.22: Macroscopic view of the dual wave. The weaves are rotated with a relative angle of 22° . (b) is the mapped result of CST and (a), at the frequency of 20.12 GHz. Note that this is an approximation. $a=1$ mm, $b/a=0.7$, $\sigma = 10^5$ S/m and $t = 80$ μm , distance between the slabs is 0.2 mm.

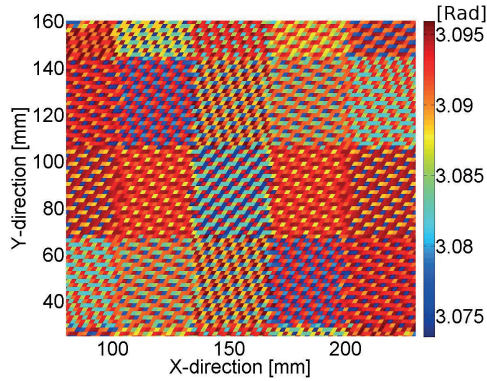


Figure 7.23: Macroscopic view of the dual wave. The weaves are rotated with a relative angle of 22° . It is the mapped result of CST and the geometrical moiré pattern, at the frequency of 20.12 GHz. Note that this is an approximation. $a=1$ mm, $b/a=0.7$, $\sigma = 10^5$ S/m and $t = 80$ μm , distance between the slabs is 0.2 mm.

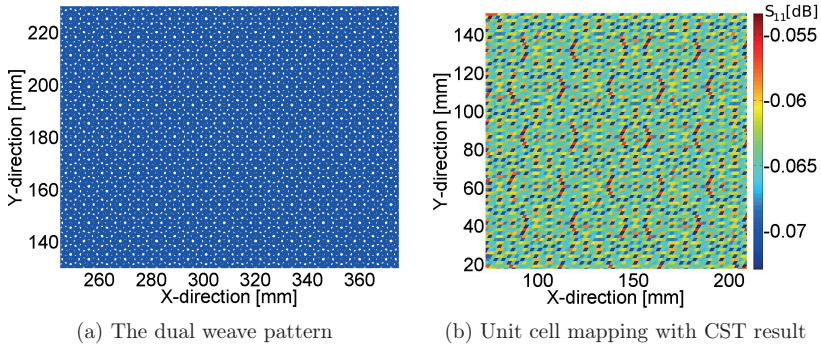


Figure 7.24: Macroscopic view of the dual wave. The weaves are rotated with a relative angle of 30° . (b) is the mapped result of CST and (a), at the frequency of 20.12 GHz. Note that this is an approximation. $a=1$ mm, $b/a=0.7$, $\sigma = 10^5$ S/m and $t = 80$ μm , distance between the slabs is 0.2 mm.

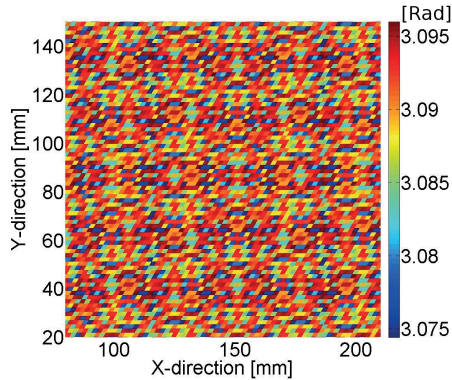
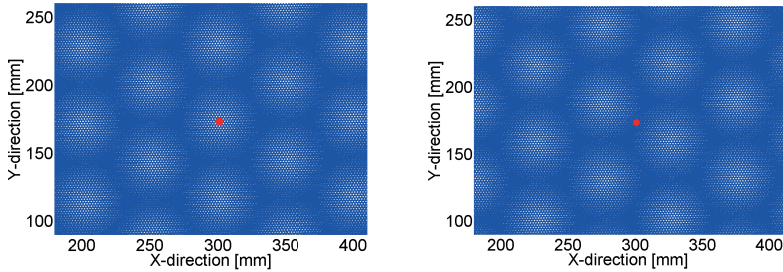


Figure 7.25: Macroscopic view of the dual wave. The weaves are rotated with a relative angle of 30° . It is the mapped result of CST and the geometrical moiré pattern, at the frequency of 20.12 GHz. Note that this is an approximation. $a=1$ mm, $b/a=0.7$, $\sigma = 10^5$ S/m and $t = 80$ μm , distance between the slabs is 0.2 mm.

7.3.3 Both relative translation and rotation

As part of the moiré pattern investigation, the pattern that occurs at a combination of relative translation and rotation was considered. The moiré pattern at a macroscopic perspective then only appeared to be translated around the point of rotation. Therefore it is enough to only study the purely rotated weaves to understand the macroscopic behaviour of the combined translated and rotated dual weaves. An example of this is presented in Figure 7.26.



(a) Relative rotation=2 degrees, x-translation=0, mm y-translation=0 mm. (b) Relative rotation=2 degrees, x-translation= $a/2$, y-translation= $a\frac{\sqrt{3}}{2}$.

Figure 7.26: The moiré pattern at two different translations, but with the same rotation angle. The red dot marks the center of rotation. The pattern that appear are very similar but with a translation.

7.4 Parametric sweep of the hole size in the dual weave case

Since it was shown in Figure 7.15 and 7.13 that a sufficient reflection coefficient is achieved by a dual weave it is interesting to see how big one can make the hexagon shaped hole. To test this a parametric sweep of the b/a ratio was conducted of a dual weave with coincident holes. That is no relative rotation or translation. The result is presented in Figure 7.27. From this result one can conclude that biggest possible ratio is b/a of 0.7156.

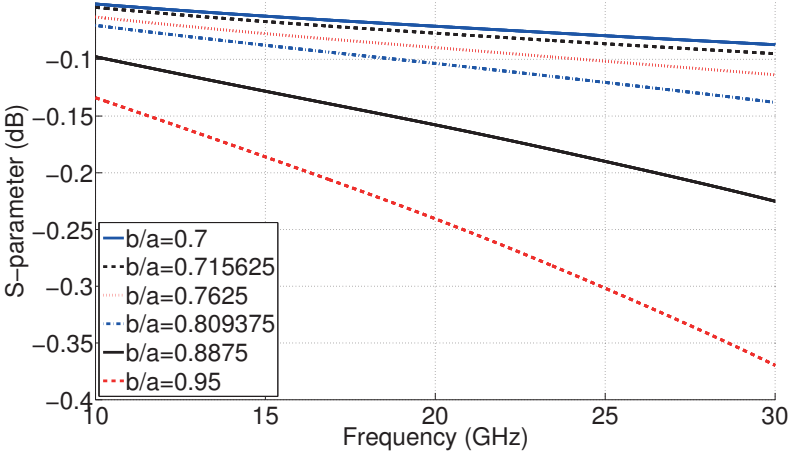


Figure 7.27: S_{11} parameters as function of frequency at different hole size ratios (b/a) in the dual wave case when the holes are coincident. The other parameters are $a = 1$ mm, $\sigma = 10^5$ S/m, $t = 80$ μ m and $\text{slabDist}=0.2$ mm. The result was computed in CST.

7.5 Further observations

By placing two parallel slabs close to each other one creates a Fabry-Perot resonator. A Fabry-Perot resonator consists of two parallel semi reflective surfaces separated by a distance. When the distance between these reflective surfaces is half a wavelength, high transmission is obtained for this wavelength [13, p. 203-208].

In the dual weave one can observe a decrease in the reflection when the distance between the weaves are a multiple of half a wavelength. The frequency for which the reflection decreases can be predicted by (7.8).

$$f = \frac{c}{n2t_1 + 2t_2} \quad (7.8)$$

where c is the speed of light, $n = \sqrt{\mu_r \epsilon_r} \approx \sqrt{2}$ is the refractive index, t_1 is the thickness of the first slab and t_2 is the distance in-between the slabs.

It is thus very important to consider the distance between the slabs when designing the dual weave. Some examples of this phenomena are plotted in Figures 7.28 - 7.29. The effect of this phenomena cease to be present within the frequency span of 10-30 GHz at distances between the slab of 3.4 mm or less. To validate this a sweep for closer slab distances was done and is presented in Figure 7.30.

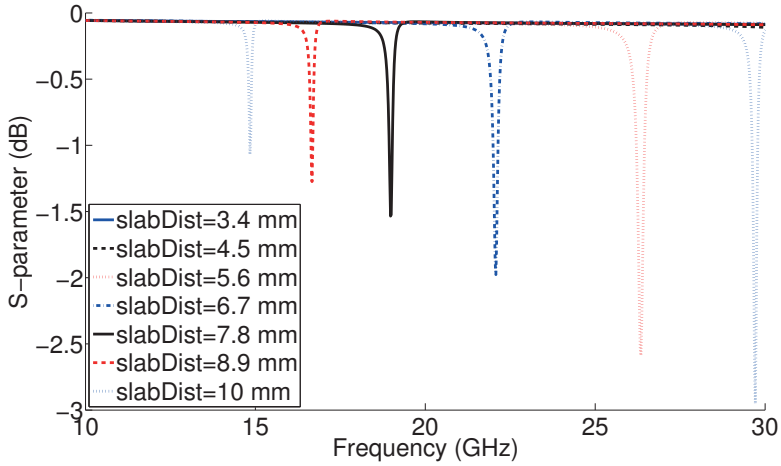


Figure 7.28: S_{11} parameters as function of frequency at different slab distances between the layers in the dual wave with periodic boundary conditions in the slab model. The other parameters are $a = 1$ mm, $b/a=0.7$, $\sigma = 10^5$ S/m, $t = 80$ μm . The result was computed in CST.

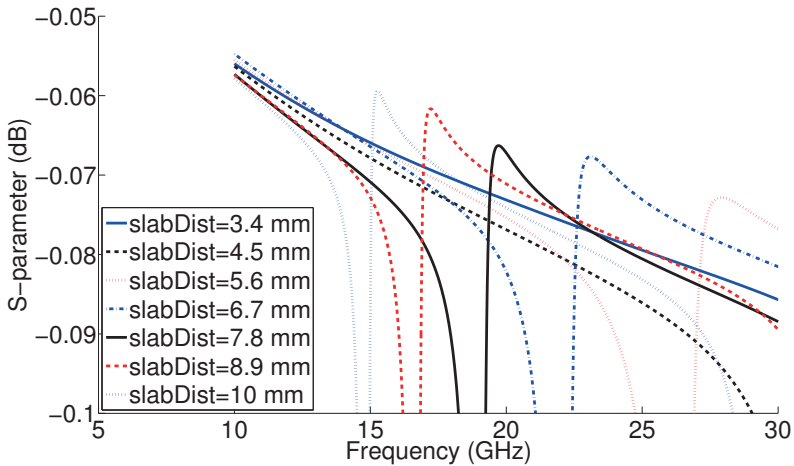


Figure 7.29: Same as Figure 7.28, but zoomed. S_{11} parameters as function of frequency at different slab distances between the layers in the dual wave with periodic boundary conditions in the slab model. The other parameters are $a = 1$ mm, $b/a=0.7$, $\sigma = 10^5$ S/m, $t = 80$ μm . The result was computed in CST.

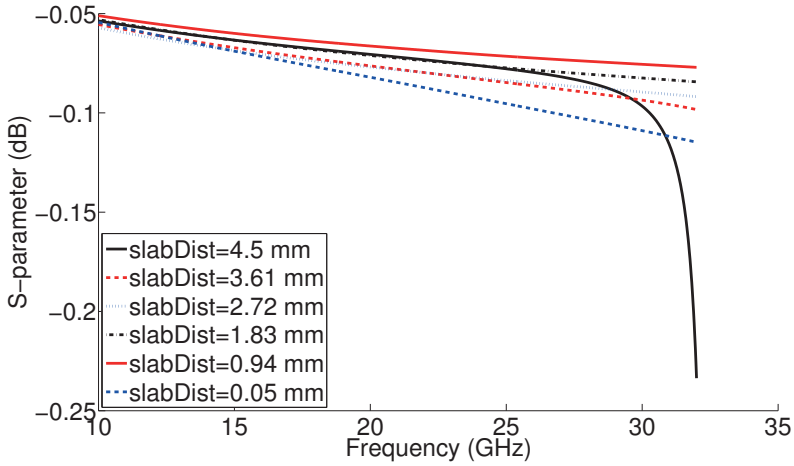


Figure 7.30: Very similar plot as Figure 7.28, but with a closer distance between the slabs.

7.6 Summary

By introducing a second wave one easily obtains the higher required reflection. However, the new geometry causes some issues and there are some difficulties in modelling the dual wave properly.

It is rather crucial to consider the distance between the weaves. If it is chosen too large an undesired high transmission can occur.

A new macroscopic moiré periodicity is created for some relative rotations in the dual wave. The periodicity as a function of the relative rotation had a rather complicated appearance. By choosing a relative rotation angle, φ , that fulfils $\cos(\varphi) \notin \mathbb{Q}$ one avoids the existence of a macroscopic periodicity. This periodicity can be looked upon as quasi periodic. Based on an approximation method it seems that the moiré pattern does not change the macroscopic behaviour of the reflector substantially.

By only translating the weaves relative to each other one obtains an equally relative phase shift and reflection all over the reflector. One can also choose a relative rotation of eg. 30° by which one obtains a relatively equally distributed relative phase shift and reflection coefficient, without any macroscopic periodicity.

In 7.18 to 7.25 it appears that the reflection coefficient and phase shift changes significantly in the weave, but the color legends span tight intervals of ~ 0.02 dB and ~ 0.02 rad. It can be questioned if this high accuracy obtained by mathematical simulations is applicable in the real weave or possible to measure. There are a numerous sources of modelling errors, modelling the weave. Examples of these sources are that the conductivity and the geometry of the weave is not exactly known. E.g. in Figure 5.5 it appears that changing the conductivity by a factor 2 gives rise to a change in the reflection coefficient of a few hundredths dB.

8

Parabolic reflector

The idea of this chapter is to put the result derived in the previous chapter in context of a reflector antenna and thereby visualise and compare the performance of a parabolic reflector antenna with a single tri-axial carbon fibre weave. To do this a general method to analyse a parabolic reflector antenna of arbitrary material is derived and then compared with the same calculations using physical optics (PO) for a PEC parabolic antenna. Note that all the derivations here are done for a vacuum environment, that is $\mu_r = \epsilon_r = \eta = 1$.

8.1 PO approximation for PEC parabolic shaped surface

The main idea of PO is that one only consider the enlightened surface of the reflector and that the incident electric field gives rise to currents that then radiates electromagnetic waves. This leads to two major approximations. The first approximation is that the normal component of the incident electric field is zero at the reflecting surface; $\hat{\mathbf{n}} \times \mathbf{E} = \mathbf{0}$. The other approximation is that it is only the enlightened surface that contributes to the reflected field. Thus the frequency must be reasonably high and the reflected surface must be a PEC.

In [10, p. 104-107] the far-field of a parabolic PEC reflector antenna is derived by the PO method. Here is a replication of that result conducted and in Section 8.2 a modified method derived for a non PEC case is presented. An example of a parabolic reflector is plotted in Figure 8.1.

Let a parabolic PEC reflector be fed by a dipole antenna located in the focal point. The far-field of a dipole is then (using time convention $e^{-i\omega t}$ as in [10]):

$$\mathbf{E}_i = \frac{pk^2}{\epsilon_0} \frac{e^{ikr}}{4\pi r} (\hat{\mathbf{r}}_0 \times (\hat{\mathbf{y}} \times \hat{\mathbf{r}}_0)) \quad (8.1)$$

with corresponding magnetic field:

$$\mathbf{H}_i = k\omega p \frac{e^{ikr}}{4\pi r} (\hat{\mathbf{r}}_0 \times \hat{\mathbf{y}}) \quad (8.2)$$

where p is the strength of the dipole, the wave number $k = \omega/c_0$, ω is the angular frequency, c_0 is the speed of light in vacuum, ϵ_0 is the permittivity in vacuum and $\hat{\mathbf{r}}_0$ is the direction of observation. To convert the results of this section to the time

convention used in the rest of the thesis, simply replace i by $-j$. The parabolic surface is described by:

$$x^2 + y^2 = 4F(z + F), F > 0 \quad (8.3)$$

where F is the focal distance. The parabolic reflector surface can then be described as the parametrised surface in polar coordinates by:

$$\mathbf{S}(\rho, \alpha) = \hat{\rho}\rho + \hat{z}(\rho^2/4F - F) \quad (8.4)$$

The distance from the dipole to the reflector is described by:

$$r'(\rho) = \rho^2/4F + F \quad (8.5)$$

The polar unit vectors are:

$$\begin{cases} \hat{\rho} = \hat{x} \cos \alpha + \hat{y} \sin \alpha \\ \hat{\alpha} = -\hat{x} \sin \alpha + \hat{y} \cos \alpha \end{cases} \quad (8.6)$$

$$\hat{r} = \hat{x} \sin \theta \cos \phi + \hat{y} \sin \theta \sin \phi + \hat{z} \cos \theta \quad (8.7)$$

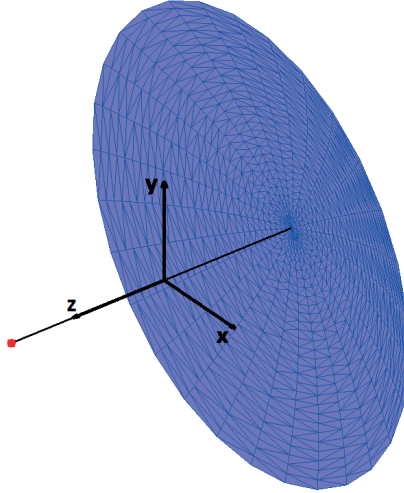


Figure 8.1: A parabolic reflector with an exterior radius of $a=0.4$ m with its focal point located at $F=0.5$ m from the midpoint.

In [10, p. 73] a definition of the far-field amplitude is introduced. The definition is given in (8.8) and is used throughout this chapter.

$$\mathbf{E}_s(\mathbf{r}) = \frac{e^{ikr}}{kr} \mathbf{F}(\hat{r}) \quad (8.8)$$

where \mathbf{E}_s is the scattered electric field. The radiated far-field for the parabolic PEC reflected can now by PO be expressed as:

$$\begin{aligned} \mathbf{F}_{fo}(\hat{\mathbf{r}}) &= -i \frac{k^2 \eta_0}{2\pi} \hat{\mathbf{r}} \times \left[\hat{\mathbf{r}} \times \iint_{S_3^+} \hat{\mathbf{n}}(\mathbf{r}') \times \mathbf{H}_i(\mathbf{r}') e^{-ik\hat{\mathbf{r}} \cdot \mathbf{r}'} dS' \right] \\ &= -i \frac{k^2 \eta_0}{2\pi} \hat{\mathbf{r}} \times \left[\hat{\mathbf{r}} \times \mathbf{I} \right] \end{aligned} \quad (8.9)$$

where $\eta_0 = \sqrt{\mu_0/\epsilon_0}$ and the integral \mathbf{I} after some derivation expressing the H-field at the parametrised reflector surface (8.4) can be written as:

$$\begin{aligned} \mathbf{I} &= \frac{k\omega p}{2F} \int_0^a \rho d\rho \int_0^{2\pi} d\alpha \frac{e^{ik(r'(\rho) - \hat{\mathbf{r}} \cdot \mathbf{S}(\rho, \alpha))}}{4\pi(r'(\rho))^2} \\ &\quad \cdot \left[\hat{\mathbf{y}} \left(S_x^2(\rho, \alpha) - 2FS_z(\rho, \alpha) \right) - \hat{\mathbf{x}} S_x(\rho, \alpha) S_y(\rho, \alpha) - \hat{\mathbf{z}} S_y(\rho, \alpha) S_z(\rho, \alpha) \right] \end{aligned} \quad (8.10)$$

The integral in (8.10) can then be computed numerically for different $\hat{\mathbf{r}}$ in (8.9), where $\hat{\mathbf{r}}(\theta, \phi)$ see (8.7).

8.2 Extension of the PO method to suit a material with high finite conductivity

8.2.1 A useful expression

In [10, p. 105] the normal vector is derived as:

$$\hat{\mathbf{n}}(\rho, \alpha) = \frac{-\hat{\rho}\rho + \hat{\mathbf{z}}2F}{\sqrt{\rho^2 + 4F^2}} \quad (8.11)$$

From (8.11) one obtains by the definition of dot product the following expression for $\theta(\rho, \alpha)$:

$$\theta(\rho, \alpha) = \arccos(\hat{\mathbf{n}}(\rho, \alpha) \cdot \hat{\mathbf{z}}) = \arccos\left(\frac{2F}{\sqrt{\rho^2 + 4F^2}}\right) = \theta(\rho) \quad (8.12)$$

which will be useful in the next section.

8.2.2 Derivation of method

Since the weave has a finite conductivity the PO presumptions will not hold. Going back to the derivation of a short wave approximation leading to the PO approximation in [10, p. 94] the following equation for the far-field is derived in the context of the scattering at a PEC surface in air ($n \approx 1$).

$$\mathbf{F}_{fo}(\hat{\mathbf{r}}) = i \frac{k^2}{4\pi} \hat{\mathbf{r}} \times \iint_{S_3^+} \left[\hat{\mathbf{n}}(\mathbf{r}') \times \mathbf{E}(\mathbf{r}') - \eta_0 \hat{\mathbf{r}} \times \left(\hat{\mathbf{n}}(\mathbf{r}') \times \mathbf{H}(\mathbf{r}') \right) \right] e^{-ik\hat{\mathbf{r}} \cdot \mathbf{r}'} dS' \quad (8.13)$$

The cross products $\hat{\mathbf{n}}(\mathbf{r}') \times \mathbf{E}(\mathbf{r}')$ and $\hat{\mathbf{n}}(\mathbf{r}') \times \mathbf{H}(\mathbf{r}')$ in (8.13) only affect the tangential fields \mathbf{E}_t and \mathbf{H}_t . At the surface of the reflector \mathbf{E}_t is described by the incident E-field and the reflected E-field characterised by the reflection dyad $\bar{\bar{\mathbf{r}}}$:

$$\mathbf{E}_t(\mathbf{r}') = \mathbf{E}_t^i(\mathbf{r}') + \bar{\bar{\mathbf{r}}} \cdot \mathbf{E}_t^i(\mathbf{r}') = (\bar{\bar{\mathbf{I}}} + \bar{\bar{\mathbf{r}}}) \cdot \mathbf{E}_t^i(\mathbf{r}') \quad (8.14)$$

Similarly, \mathbf{H}_t at the reflector is described by:

$$\mathbf{H}_t^i(\mathbf{r}') = \frac{1}{\eta_0} (\hat{\mathbf{k}}^i(\mathbf{r}') \times \mathbf{E}^i(\mathbf{r}'))_t = \bar{\bar{\mathbf{Z}}}_w^{-1} \cdot \mathbf{E}_t^i(\mathbf{r}') \quad (8.15)$$

$$\bar{\bar{\mathbf{Z}}}_w^{-1} = \eta_0 \begin{pmatrix} \cos \theta & 0 \\ 0 & \frac{1}{\cos \theta} \end{pmatrix} \quad (8.16)$$

$$\mathbf{H}_t(\mathbf{r}') = \mathbf{H}_t^i(\mathbf{r}') + \mathbf{H}_t^r(\mathbf{r}') = \bar{\bar{\mathbf{Z}}}_w^{-1} (\bar{\bar{\mathbf{I}}} - \bar{\bar{\mathbf{r}}}) \cdot \mathbf{E}_t^i(\mathbf{r}') \quad (8.17)$$

To simplify the vector integral expressions the reflector dyad $\bar{\bar{\mathbf{r}}}$ is only expressed in terms of one of the polarisations. This approximation is based on an assumption that there is not a significant difference in the reflection of the TE- and TM-polarisation and that the cross-polarisation terms are zero (which is reasonable in the carbon fibre weave case). The reflection dyad $\bar{\bar{\mathbf{r}}}$ is then written in terms of the TE-polarisation as (8.18). Note that reflection dyad can by this assumption be equally well expressed in the TM-polarisation.

$$\bar{\bar{\mathbf{r}}} = \begin{pmatrix} S_{11}(\theta(\rho)) & 0 \\ 0 & S_{11}(\theta(\rho)) \end{pmatrix} = S_{11}(\theta(\rho)) \bar{\bar{\mathbf{I}}} \quad (8.18)$$

where $\bar{\bar{\mathbf{I}}}$ is the unity dyad. This implies by inserting (8.18) in (8.17) that:

$$\begin{aligned} \mathbf{H}_t(\mathbf{r}') &= \bar{\bar{\mathbf{Z}}}_w^{-1} (\bar{\bar{\mathbf{I}}} - \bar{\bar{\mathbf{r}}}) \cdot \mathbf{E}_t^i(\mathbf{r}') = (1 - S_{11}(\theta(\rho))) \bar{\bar{\mathbf{Z}}}_w^{-1} \bar{\bar{\mathbf{I}}} \cdot \mathbf{E}_t^i(\mathbf{r}') = \\ &= (1 - S_{11}(\theta(\rho))) \mathbf{H}_t^i(\mathbf{r}') \end{aligned} \quad (8.19)$$

By inserting (8.14) and (8.19) in (8.13) one obtains:

$$\begin{aligned} \mathbf{F}_{fo}(\hat{\mathbf{r}}) &= i \frac{k^2}{4\pi} \hat{\mathbf{r}} \times \iint_{S_+^+} \left[(\bar{\bar{\mathbf{I}}} + \bar{\bar{\mathbf{r}}}) (\hat{\mathbf{n}}(\mathbf{r}') \times \mathbf{E}^i(\mathbf{r}')) \right. \\ &\quad \left. - \eta_0 \hat{\mathbf{r}} \times \bar{\bar{\mathbf{Z}}}_w^{-1} (\bar{\bar{\mathbf{I}}} - \bar{\bar{\mathbf{r}}}) (\hat{\mathbf{n}}(\mathbf{r}') \times \mathbf{E}^i(\mathbf{r}')) \right] e^{-ik\hat{\mathbf{r}} \cdot \mathbf{r}'} dS' \end{aligned} \quad (8.20)$$

By inserting (8.18) and (8.19) in (8.20) one further obtains:

$$\begin{aligned} \mathbf{F}_{fo}(\hat{\mathbf{r}}) &= i \frac{k^2}{4\pi} \hat{\mathbf{r}} \times \iint_{S_+^+} \left[(1 + S_{11}(\theta(\rho))) (\hat{\mathbf{n}}(\mathbf{r}') \times \mathbf{E}^i(\mathbf{r}')) \right. \\ &\quad \left. - \eta_0 \hat{\mathbf{r}} \times (1 - S_{11}(\theta(\rho))) (\hat{\mathbf{n}}(\mathbf{r}') \times \mathbf{H}^i(\mathbf{r}')) \right] e^{-ik\hat{\mathbf{r}} \cdot \mathbf{r}'} dS' \end{aligned} \quad (8.21)$$

The expression in (8.21) can then be divided into two different integral expressions:

$$\begin{aligned} \mathbf{F}_{fo}(\hat{\mathbf{r}}) &= i \frac{k^2}{4\pi} \hat{\mathbf{r}} \times \iint_{S_+^+} \left[(1 + S_{11}(\theta(\rho))) (\hat{\mathbf{n}}(\mathbf{r}') \times \mathbf{E}^i(\mathbf{r}')) \right] e^{-ik\hat{\mathbf{r}} \cdot \mathbf{r}'} dS' \\ &\quad - i \frac{k^2 \eta_0}{4\pi} \hat{\mathbf{r}} \times \left[\hat{\mathbf{r}} \times \iint_{S_+^+} \left(\hat{\mathbf{n}}(\mathbf{r}') \times (1 - S_{11}(\theta(\rho))) \mathbf{H}^i(\mathbf{r}') \right) e^{-ik\hat{\mathbf{r}} \cdot \mathbf{r}'} dS' \right] \end{aligned} \quad (8.22)$$

(8.22) is then by previous notation written as:

$$(8.22) = i \frac{k^2}{4\pi} \left[\hat{\mathbf{r}} \times \mathbf{I}_E \right] - i \frac{k^2 \eta_0}{4\pi} \hat{\mathbf{r}} \times \left[\hat{\mathbf{r}} \times \mathbf{I}_H \right] \quad (8.23)$$

where \mathbf{I}_H is:

$$\begin{aligned} \mathbf{I}_H &= \frac{k\omega p}{2F} \int_0^a \rho d\rho \int_0^{2\pi} d\alpha (1 - S_{11}(\theta(\rho))) \frac{e^{ik(r'(\rho) - \hat{\mathbf{r}} \cdot \mathbf{S}(\rho, \alpha))}}{4\pi(r'(\rho))^2} \\ &\quad \cdot \left[\hat{\mathbf{y}} \left(S_x^2(\rho, \alpha) - 2FS_z(\rho, \alpha) \right) - \hat{\mathbf{x}}S_x(\rho, \alpha)S_y(\rho, \alpha) - \hat{\mathbf{z}}S_y(\rho, \alpha)S_z(\rho, \alpha) \right] \end{aligned} \quad (8.24)$$

which is very similar to (8.10). To formulate \mathbf{I}_E properly a similar derivation as the one conducted in [10, p.106] is performed. $\mathbf{E}_i(\rho, \alpha)$ originating from the dipole can be expressed by:

$$\mathbf{E}_i(\rho, \alpha) = \frac{pk^2}{\epsilon_0 4\pi} \frac{e^{ikr'(\rho)}}{r'(\rho)} (\hat{\mathbf{k}}_i \times (\hat{\mathbf{y}} \times \hat{\mathbf{k}}_i)) \quad (8.25)$$

where:

$$\hat{\mathbf{k}}_i = \frac{\hat{\rho}4F\rho + \hat{\mathbf{z}}(\rho^2 - 4F^2)}{\rho^2 + 4F^2} \quad (8.26)$$

$$\hat{\mathbf{y}} = \hat{\rho} \sin \alpha + \hat{\alpha} \sin \alpha \quad (8.27)$$

This gives by a vector identity that the parametrised \mathbf{E}_i is:

$$\begin{aligned} \mathbf{E}_i(\rho, \alpha) &= \frac{pk^2}{\epsilon_0 4\pi} \frac{e^{ikr'(\rho)}}{r'(\rho)} \left[\hat{\rho} \left((4F^2 + \rho^2) - \frac{(4F\rho)^2}{(\rho^2 + 4F^2)^2} \right) \sin \alpha + \right. \\ &\quad \left. + \hat{\alpha} (4F^2 + \rho^2) \cos \alpha - \hat{\mathbf{z}} \frac{4F\rho(\rho^2 - 4F)}{(4F^2 + \rho^2)^2} \right] \end{aligned} \quad (8.28)$$

The crossproduct $\hat{\mathbf{n}} \times \hat{\mathbf{E}}_i$ is then:

$$\begin{aligned} \hat{\mathbf{n}}(\rho, \alpha) \times \hat{\mathbf{E}}_i(\mathbf{S}((\rho, \alpha))) &= \frac{pk^2}{\epsilon_0 (4F)^{\frac{7}{2}}} \frac{e^{ikr'(\rho)}}{4\pi(r'(\rho))^{\frac{7}{2}}} \left[-\hat{\mathbf{x}}2F [2\sin^2 \alpha \rho^2 (\rho^2 - 4F) + ((4F^2 + \rho^2)^3 - (4F\rho)^2)] \right. \\ &\quad \left. + \hat{\mathbf{y}}4F\rho \sin(2\alpha) [-4F^2\rho + \frac{\rho}{2}(\rho^2 - 4F)] \right. \\ &\quad \left. + \hat{\mathbf{z}}\rho \cos \alpha [(4F\rho)^2 - (4F^2 + \rho^2)^3 + \sin^2 \alpha (4F\rho)^2] \right] \end{aligned} \quad (8.29)$$

Note that a surface element in the integral \mathbf{I}_E is:

$$\left| \frac{\partial \mathbf{S}}{\partial \rho} \times \frac{\partial \mathbf{S}}{\partial \alpha} \right| = \rho \sqrt{r'(\rho)/F} \quad (8.30)$$

Similarly to (8.24) \mathbf{I}_E can then be expressed as:

$$\begin{aligned} \mathbf{I}_E = & \frac{pk^2}{\epsilon_0 F^3 4^{5/2}} \int_0^a \rho d\rho \int_0^{2\pi} d\alpha (1 + S_{11}(\theta(\rho))) \frac{e^{ik(r'(\rho) - \hat{r} \cdot \mathbf{S}(\rho, \alpha))}}{4\pi(r'(\rho))^3} \\ & \cdot \left[-\hat{\mathbf{x}} 2F [2 \sin^2 \alpha \rho^2 (\rho^2 - 4F) + ((4F^2 + \rho^2)^3 - (4F\rho)^2)] \right. \\ & \quad + \hat{\mathbf{y}} 4F \rho \sin(2\alpha) \left[-4F^2 \rho + \frac{\rho}{2} (\rho^2 - 4F) \right] \\ & \quad \left. + \hat{\mathbf{z}} \rho \cos \alpha [(4F\rho)^2 - (4F^2 + \rho^2)^3 + \sin^2 \alpha (4F\rho)^2] \right] \quad (8.31) \end{aligned}$$

(8.22) can now be computed by similar numerical methods as for the PO parabolic reflector case (8.9).

8.3 Results

In order for (8.18) to hold the presumption that there is not a big difference in the reflection coefficient of the TE and TM polarisation as a function of the incident angle θ must be true. Consider the parametric sweep chapter, Figure 5.11, where the different reflection coefficients for the TE and TM polarisation as a function of frequency are plotted for different incident angles respectively for the fine structure model. There is a dependency on the incident angle. Since it is rather computationally heavy to get a higher discretisation in the sweeping angle for the fine structure model the incident angle θ was swept for the slab model at 11 GHz. The results are presented in Figure 8.2 and it appears that the reflection coefficients of the TE- and TM-polarisation diverge. However, from (8.12) one realises that the angle of incidence at the parabolic surface θ for a reflector with the radius $a = 0.4$ m and focal distance of $F = 0.5$ m will not exceed 22° . The assumption that the reflection coefficients of the TE- and TM-polarisation are equal is thus valid for the carbon fibre weave at 11 GHz.

An analytical expression for the parameter $S_{11}(\theta)$ is then approximated by exporting 1001 points of $S_{11}(\theta)$ values computed in CST for the slabmodel at the frequency of 11 GHz in the interval $\theta \in [0^\circ 80^\circ]$ into MATLAB, where a fourth order polynomial least square approximation is performed ("polyfit").

It appears then that $|S_{11}(\theta)|$ and $\arg(S_{11}(\theta))$ are monotonically increasing functions in the interval of $[0^\circ 80^\circ]$. Thus lies the maximum and minimum point at the boundaries. Considering the interval of $[0^\circ 21.8^\circ]$:

$$\begin{aligned} S_{11}(0) &= -0.991802581047211 + 0.041554582726335i \Rightarrow |S_{11}(0)| = 0.992672727094620 \\ S_{11}(21.8) &= -0.992483392964098 + 0.038587200659386i \Rightarrow |S_{11}(21.8)| = 0.993233234121903 \end{aligned}$$

This implies that the terms $(1 + S_{11}(\theta)) \approx 0$ and $(1 - S_{11}(\theta)) \approx 2$ in (8.21). This means that the PO approximation based on a PEC is a reasonable approximation for

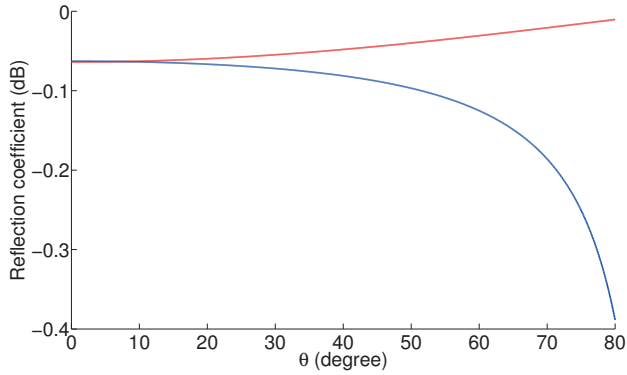


Figure 8.2: The S_{11} parameter as function of incident angles for the TE-polarisation (red) and TM-polarisation (blue) in the slab model at 11 GHz. The parameters are $a = 1$ mm, $b/a = 0.7$, $\sigma = 10^5$ S/m, $t = 80$ μ m. The results were computed in CST.

the parabolic carbon fibre weave reflector with a high reflection. Which seems to be consistent with the result computed by (8.9) and (8.22) presented in Figures 8.3 to 8.5.

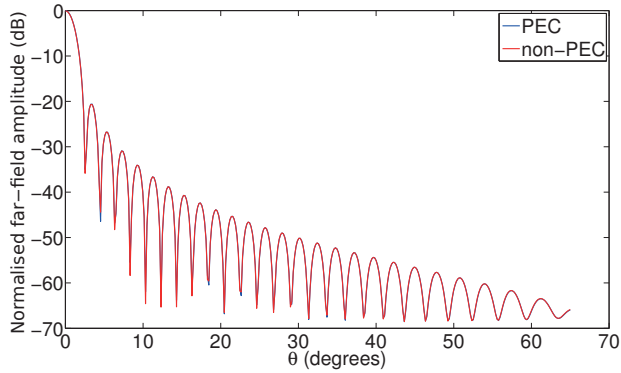


Figure 8.3: A comparison of the normed amplitude of the far-field E-field as function of incident angles θ for a parabolic reflector with an exterior radius of $a=0.4$ m and with the focal point $F=0.5$ at 11 GHz for the PEC case and for the slab model weave.

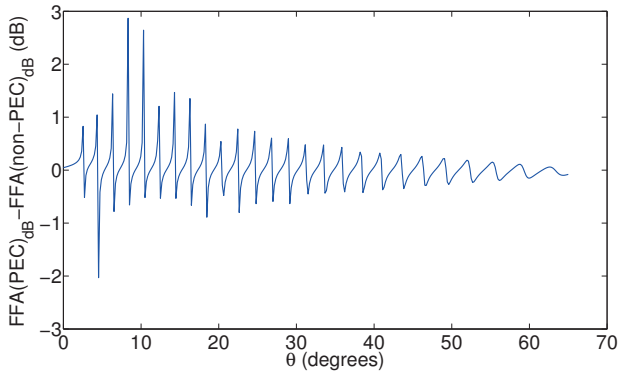
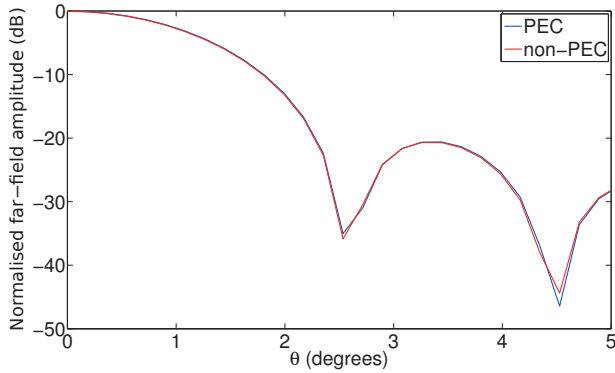


Figure 8.4: The difference in dB of the far-field amplitude in Figure 8.3.

Figure 8.5: Similar to Figure 8.3, but zoomed in at the interval $\theta \in [0, 5]$ degrees.

8.4 Summary

A carbon fibre weave with a reflection coefficient of -0.1 dB or higher, shaped as a parabolic reflector with the exterior radius of 0.4 m and the focal distance of 0.5 m, will perform as well as a PEC reflector of the same shape at 11 GHz.

9

Conclusions

The thesis set out to investigate if a tri-axial carbon fibre weave can meet the electromagnetic reflection performance required for a reflector antenna in the context of an unknown geometrical constraint based on the acoustical performance of the weave. The reflector antenna is modelled in two steps. First the reflector surface is modelled as an infinite 2D plane, which by symmetry and periodicity boundaries is narrowed down to a small finite unit cell. The obtained reflection coefficient values are then used in a modified physical optics approximation to model the performance of a parabolic reflector. The outcome useful for this project is summarised in Section 9.1 below.

Computational improvements

It could be concluded that the smallest possible element that correctly can model the entire weave is the unit cell for the fine structure model (see Figure 1.3a.). In the slab model the unit cell shape could be reduced to half the size (see Figure 4.8). Unfortunately, this insight does not reduce the computational load significantly compared to any of the previously known models.

Parameters of a single weave layer

Doing some various parameter sweeps for the weave one could conclude that the reflection coefficient is independent of the azimuthal angle, but is highly dependent on the normal incident angle to the weave within the frequency range of 10-30 GHz. Furthermore, the reflection coefficient differs for the TE and TM polarisations at different normal incident angles (θ).

In the parameter sweep it could also be concluded that the weave meet the design requirement of a reflection coefficient for a part of the frequency range, but not for the whole interval with the given geometry ($a=1$ mm, $b/a=0.7$, $t=80$ μm , $\sigma = 10^5$ S/m). However, it is possible to reach the design requirements if one makes the unit cell smaller and thicker and/or increase the conductance of the weave. The conclusions of the weave parameters are summarised in Table 5.1.

Possible improvement methods

PEC coating

PEC coating is an easy method to increase the reflection of the single weave, but is not preferable due to the PIM effect occurring at high power feed, and the cost of the coating.

Dual weave layers

Another method to increase the performance of the weave is to take two weaves and put them on top of each other. Doing so leads to some quite interesting discoveries. It is crucial to consider the distance between the weaves. If it is chosen too large (> 2.5 mm for the frequency range 10-30 GHz) an undesired high transmission can occur.

By trying to understand how moiré patterns occur and behave it was discovered that the periodicity in the pattern has a rather complicated behaviour. The periodicity as function of the rotational angle turns out to be a discrete function, which has no values at irrational $\cos \phi \notin \mathbb{Q}$, where ϕ is the rotational angle. However, the irrational quotas can be approximated by rational numbers, e.g. by continuous fraction, implying that there occurs quasi periodicity in the dual weave.

It could be concluded that having two weaves (of $a=1$ mm, $b/a=0.7$, $t=80\mu\text{m}$, $\sigma = 10^5$ S/m) increased the performance to meet the design requirement throughout the entire frequency range. By choosing a quasi periodic moiré pattern one can avoid having any periodicity in the phase change over the weave surface.

Parabolic reflector visualisation

A comparison of the far-field amplitude of a PEC reflector computed by PO and the far-field amplitude of a reflector with a scattering parameter of the design requirement, $S_{11} = -0.1$ dB, at 11 GHz exhibited no significant difference.

9.1 Conclusions relevant for the co-optimisation project

There are typically three alternatives to reach the electromagnetic design requirement of a reflection coefficient of -0.1 dB:

- Increase the conductivity to $\sim > 1.5 \cdot 10^5$ S/m and keep the design $a=1$ mm, $b/a=0.7$, $t=80 \mu\text{m}$.
- Make the unit cell denser and thicker by minimising a and increasing t . Keep $b/a=0.7$, $\sigma = 10^5$ S/m.
- Add two weaves with the dimensions $a=1$ mm, $b/a=0.7$, $t=80 \mu\text{m}$, $\sigma = 10^5$ S/m. No translation or rotation is needed.

Bibliography

- [1] Northrop Grumman. <http://www.northropgrumman.com/BusinessVentures/AstroAerospace/Products/Documents/pageDocs/Parametrics.pdf>, 2014. [Online; accessed August 2014].
- [2] Toho Tenax. http://www.tohotenax.com/tenax/en/products/st_property.php, 2014. [Online; accessed August 2014].
- [3] E. Collett. *Polarized Light fundamentals and applications*. Marcel Dekker, inc, 1993.
- [4] J. Daintith. *A Dictionary of Physics*. Oxford Paperback Reference. OUP Oxford, 2009.
- [5] J.-G. Dumoulin. Passive intermodulation and its effect on space programs. In *Screening Effectiveness Measurements (Ref. No. 1998/452)*, IEE Colloquium on, pages 2/1–210, May 1998.
- [6] A. Ericsson, D. Sjöberg, and N. Wellander. Electromagnetic homogenization of reflector antenna surfaces. Technical report, Department of Electrical and Information Technology, Faculty of Engineering, LTH, Lund University, SE-221 00, Lund Sweden, 2014.
- [7] A. Galehdar, K. Nicholson, W. Rowe, and K. Ghorbani. The conductivity of uni-directional and quasi isotropic carbon fiber composites. In *Microwave Conference (EuMC), 2010 European*, pages 882–885, Sept 2010.
- [8] S. Gona, P. Tomasek, and V. Kresalek. Measurement of conductivity of carbon fibers at microwave frequencies. In *Radioelektronika (RADIOELEKTRONIKA), 2013 23rd International Conference*, pages 68–71, April 2013.
- [9] W. Imbriale, S. Gao, and L. Boccia. *Space Antenna Handbook*. Wiley, 2012.
- [10] G. Kristensson. *Spridningsteori med antenntillämpningar*. 1999.
- [11] A. Miura and M. Tanaka. A mesh reflecting surface with electrical characteristics independent on direction of electric field of incident wave. In *Antennas and Propagation Society International Symposium, 2004. IEEE*, volume 1, pages 33–36 Vol.1, June 2004.
- [12] K. Pontoppidan and H.-H. Viskum. Electrical properties of triaxially woven fabrics for reflector antennas. *Antennas and Propagation Society International Symposium, 2003. IEEE*, 2:774 – 777, 2003.
- [13] F. Smith and J. Thomson. *Optics*. Manchester Physics Series. Wiley, 1988.
- [14] T. Stanev. *High Energy Cosmic Rays*. Praxis Publishing LTD, 2010.

- [15] W.-C. Tang and C. Kudsia. Multipactor breakdown and passive intermodulation in microwave equipment for stellite applications. In *Military Communications Conference, 1990. MILCOM '90, Conference Record, A New Era. 1990 IEEE*, pages 181–187 vol.1, Sep 1990.

Appendices

A

Geometry appendix

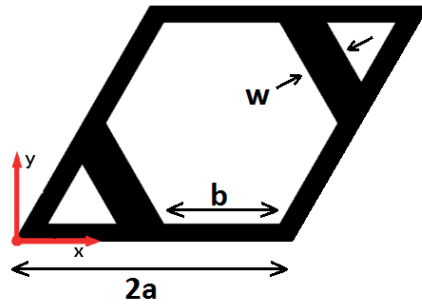


Figure A.1: The unit cell of the slab model with chosen parameter names.

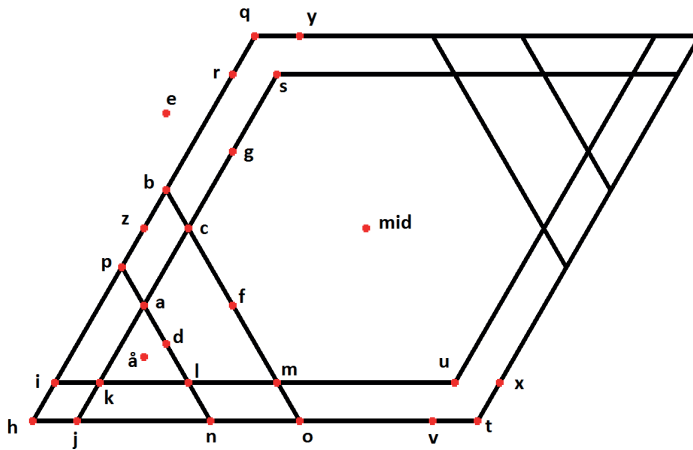


Figure A.2: Names of different points in and around the unit cell.

Name	x-coordinate	y-coordinate
a	$\frac{a}{2}$	$\sqrt{3}(b - \frac{a}{2})$
b	$a - \frac{b}{2}$	$\sqrt{3}(a - \frac{b}{2})$
c	$\frac{3a}{2} - b$	$\frac{a\sqrt{3}}{2}$
d	$\frac{3b}{4}$	$\frac{b\sqrt{3}}{4}$
e	$\frac{3b}{4}$	$\sqrt{3}(a - \frac{b}{4})$
f	$\frac{3}{2}(a - \frac{b}{2})$	$\frac{\sqrt{3}}{2}(a - \frac{b}{2})$
g	$\frac{3}{2}(a - \frac{b}{2})$	$\frac{\sqrt{3}}{2}(a + \frac{b}{2})$
h	0	0
i	$\frac{a-b}{2}$	$\frac{w}{2}$
j	$a - b$	0
k	$\frac{3}{2}(a - b)$	$\frac{w}{2}$
l	$\frac{3b-a}{2}$	$\frac{w}{2}$
m	$\frac{3a-b}{2}$	$\frac{w}{2}$
n	b	0
o	$2a - b$	0
p	$\frac{b}{2}$	$\frac{b\sqrt{3}}{2}$
q	a	$a\sqrt{3}$
r	$\frac{a+b}{2}$	$\frac{\sqrt{3}}{2}(a + b)$
s	$\frac{3a-b}{2}$	$\frac{(a+b)\sqrt{3}}{2}$
t	$2a$	0
u	$\frac{3a+b}{2}$	$\frac{w}{2}$
v	$a + b$	0
x	$\frac{5a-b}{2}$	$\frac{w}{2}$
y	$2a - b$	$a\sqrt{3}$
z	$\frac{a}{2}$	$\frac{a\sqrt{3}}{2}$
â	$\frac{a}{2}$	$\frac{a}{2\sqrt{3}}$
mid point	$\frac{3a}{2}$	$\frac{a\sqrt{3}}{2}$

Table A.1: The coordinates of the points in Figure A.2 in the coordinate system and with parameter names of Figure A.1.

B

Curls in the electric field in the slab model

During the project when the electric field lines were plotted, a curl phenomena occurring at different frequencies in the slab model was discovered, see Figure B.1. An idea that came up discussing this was that the curls could be due to that the wavelength in the material is of the same dimension as the unit cell, causing some sort of resonance behaviour. The wavelength in the material can be expressed by for the case $\sigma \gg \omega\epsilon$, given $\mu_r = 1$ to:

$$\lambda = \frac{2\pi}{\sqrt{\frac{\omega\mu\sigma}{2}}} \tag{B.1}$$

However, nothing certain could be concluded about a resonance frequency. The curls didn't appear in the fine structure model (see Figure B.2), where the difference is that the fine structure model only conducts along its string and the slab in every direction. This could be the reason for the curls and since the fine structure is a more correct model of the actual wave the phenomena in the slab model is looked upon as a model approximation error through out this report.

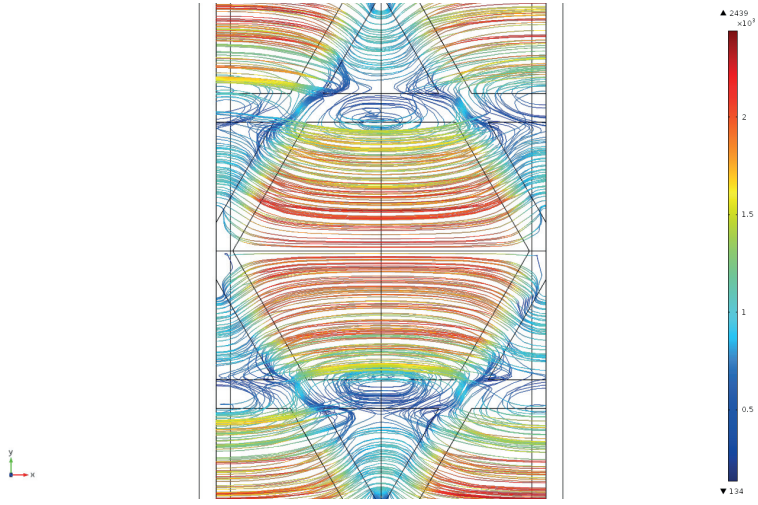


Figure B.1: The projection of the electric field lines in the xy -plane for the slab model when $b/a=0.9$, $a=1$ mm, $\sigma = 10^4$ S/m, $f=10$ GHz, x polarised excitation.

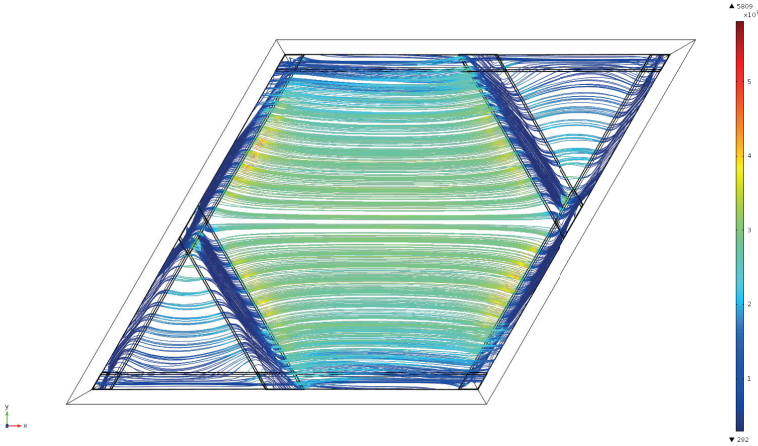


Figure B.2: The projection of the electric field lines in the xy -plane for the fine structure model when $b/a=0.9$, $a=1$ mm, $\sigma = 10^4$ S/m, $f=10$ GHz, x polarised excitation.



LUND
UNIVERSITY

Series of Master's theses
Department of Electrical and Information Technology
LU/LTH-EIT 2015-428

<http://www.eit.lth.se>